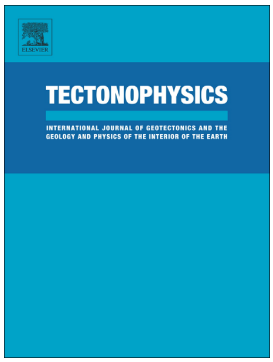

Correlation of paleoearthquake records at multiple sites along the southern Yangsan Fault, Korea: Insights into rupture scenarios of intraplate strike-slip earthquakes

Taehyung Kim, Jin-Hyuck Choi, Youngbeom Cheon, Tae-Ho Lee, Namgwon Kim, Hoil Lee, Chang-Min Kim, Yire Choi, Hankyung Bae, Young-Seog Kim, Chung-Ryul Ryoo, Yann Klinger

PII: S0040-1951(23)00115-4

DOI: https://doi.org/10.1016/j.tecto.2023.229817

Reference: TECTO 229817

To appear in: *Tectonophysics*

Received date: 18 November 2022

Revised date: 10 March 2023

Accepted date: 11 March 2023

Please cite this article as: T. Kim, J.-H. Choi, Y. Cheon, et al., Correlation of paleoearthquake records at multiple sites along the southern Yangsan Fault, Korea: Insights into rupture scenarios of intraplate strike-slip earthquakes, *Tectonophysics* (2023), https://doi.org/10.1016/j.tecto.2023.229817

Correlation of paleoearthquake records at multiple sites along the southern Yangsan Fault, Korea: Insights into rupture scenarios of intraplate strike-slip earthquakes

Taehyung Kim[1], Jin-Hyuck Choi[1], Youngbeom Cheon[1,*], Tae-Ho Lee[1], Namgwon Kim[2], Hoil Lee[1], Chang-Min Kim[1], Yire Choi[1], Hankyung Bae[1,3], Young-Seog Kim[4], Chung-Ryul Ryoo[1], Yann Klinger[5]

[1]*Active Tectonics Research Center, Korea Institute of Geosciences and Mineral Resources, Daejeon 34132, Republic of Korea*

[2]*Department of Civil and Environmental Engineering, University of Strathclyde, Galasgow G11XJ, UK*

[3]*Department of Geology, Kangwon National University, Chuncheon 24341, Republic of Korea*

[4]*Department of Earth and Environmental Sciences, Pukyong National University, Busan 48513, Republic of Korea*

[5]*Université de Paris Cité, Institut de physique du globe de Paris, CNRS, Paris, France*

Abstract

The construction of spatiotemporal models of earthquake occurrence for intraplate areas is challenging due to the low deformation rates in these areas. In this study, we conducted paleoseismological investigations along the southern Yangsan Fault (SYF), a typical low-deformation-rate fault, on the Korean Peninsula. The SYF is distinct from the northern Yangsan Fault (NYF), and the boundary between them is located at the junction between the NNE-striking YF and another major structure, the NNW-striking Ulsan Fault (UF), which branches off from the YF. Paleoseismological trenches at four sites along the SYF indicate that this fault section has not ruptured during the Holocene, in contrast to the NYF and UF. In detail, surface ruptures along the studied section of the SYF occurred during three different time periods, as inferred from stratigraphy and radiocarbon dating: 74 to 49 ka at two sites, 39 to 35 ka at another site, and 28,000 cal yr BP (or 30 ka considering the OSL age) to 16 ka at all sites. These results suggest two alternative rupture scenarios for the timing of paleoearthquakes along the studied fault section during the Late Pleistocene: (1) full rupture along the entire studied section during each earthquake event, or (2) multiple partial ruptures along the two structurally distinguishable parts of the studied fault section, that is, the Wolsan–Miho and Inbo north–Inbo sections. We conclude that geometric discontinuities of the long-lived YF system in the Korean Peninsula intraplate region have played an important role in controlling recent spatiotemporal rupture behavior.

Keywords: intraplate area, southern Yangsan Fault, rupture scenario, partial rupture, geometric discontinuity

1. Introduction

One of the critical issues in the field of earthquake hazards, which encompasses aspects such as paleoseismology, earthquake forecasting, and seismic design, is to define a model of occurrence for earthquakes involving surface rupture (e.g., Thatcher and Rundle, 1979; Schwartz and Coppersmith, 1984; Zielke et al., 2015). Geomorphic and paleoseismological investigations are one of the main tools used to establish models of long-term earthquake recurrence, as evidence for surface-rupturing earthquakes is recorded both on the surface and within shallow-subsurface geological strata (Keller and Pinter, 2001; Burbank and Anderson, 2013). The distribution of offset geomorphic markers contributes to the determination of spatial parameters of paleoearthquakes, such as rupture length, cumulative displacement, and the amount of slip per event (e.g., Choi et al., 2018). Paleoseismological trenches can give further temporal information on large paleoearthquakes, such as the number of events and recurrence intervals (e.g., Grant and Sieh, 1994; Rockwell et al., 2009; Scharer et al., 2014; Elliott et al., 2018).

Large earthquakes in intraplate regions can be more damaging than those in interplate regions because communities in the former regions are less prepared due to sparse information about past earthquakes and a lack of experience of seismic hazards (Liu et al., 2011; England and Jackson, 2011). Moreover, the spatiotemporal behavior of intraplate faults, because the time between successive earthquakes can be extremely long in regard to our ability to decipher geological record, is more difficult to characterize. Hence, variable processes have been proposed, from random pattern and/or clustering (quasi)periodic behavior, with no emerging general picture (Berryman et al., 2012; Calais, 2016; William et al., 2017; Bollinger et al., 2021).

The Korean Peninsula has long been considered a stable intraplate region with low seismicity (Fig. 1a) on the basis of the absence of historical and instrumental records of

destructive surface-rupturing earthquakes. However, a recent moderate earthquake (the 2016 M_w 5.5 Gyeongju earthquake), as well as historical records and paleoseismological investigations along the Yangsan Fault (YF; Fig. 1b and c), the largest fault structure in SE Korea, together show that this fault is one of the main seismogenic faults on the Korean Peninsula (e.g., Lee and Jin, 1991; Kyung, 2003; Lee et al., 2015; Kim et al., 2017a; Cheon et al., 2020a; Song et al., 2020; Ko et al., 2022). Despite the excavation of several paleoseismological trenches along the YF, the data remain too limited to correlate paleoearthquake ruptures across different trench sites to determine whether or not different parts of a specific fault have ruptured simultaneously. This approach is especially challenging along the YF because geomorphological evidence may have been destroyed or substantially degraded by surface processes or anthropogenic activities during the long inter-seismic period, making it difficult to accurately assess the behavior of the fault. Therefore, it is not easy to trace surface ruptures and to acquire sufficient paleoseismological information from trenching surveys and geomorphic observations to constrain earthquake history with the desired level of accuracy.

Here, we present new paleoseismological observations on surface-rupturing events along the southern YF (SYF; Fig. 2a and b). Although the studied section is located close to the epicenter of the 2016 Gyeongju Earthquake (M_w 5.5; Kim et al., 2017a, 2017b), few paleoseismological studies have been conducted along this fault section. Our main purpose is to determine the spatiotemporal distribution of surface ruptures for multiple strike-slip earthquakes along the southern YF and along the entire YF during the late Quaternary, as well as to assess the main factors controlling this distribution. First, we describe detailed geomorphic, stratigraphic, and structural features of paleoearthquake surface ruptures at three trench sites. We then combine these results with previously published results for the Inbo (IB) trench site (Cheon et al., 2020a). We further discuss (1) earthquake kinematics inferred from

stratigraphic features and (2) the spatiotemporal distribution of paleoearthquakes along the YF.

2. Study area

2.1. Seismotectonic setting

The Korean Peninsula is located in the eastern part of the Eurasian plate, more than 500 km from the Eurasia–Pacific plate boundary (Fig. 1a). The tectonic stress condition of the peninsula is dependent on the interaction between both the subducting Pacific and Philippine Sea plates and the collision of the northward-moving Indian plate with the Eurasian plate (Yin, 2010). Various investigations of the present tectonic stress, including those involving hydrofracturing/over-coring (e.g., Haimson et al., 2003; Bae et al., 2008; Chang et al., 2010; Kim et al., 2021), focal mechanisms (e.g., Park et al., 2007; Hoe and Kyung, 2008; Back et al., 2011; Choi et al., 2012a; Kuwahara et al., 2021), and fault-slip analyses (e.g., Park et al., 2006; Kim et al., 2016), indicate an ENE–WSW-trending maximum horizontal stress.

Short-term geodetic data, such as global positioning system (GPS) data derived from the recently installed permanent Korean GPS network, show that the Korean Peninsula is moving toward the southwest at a rate of 1 to 5 mm/yr relative to the Eurasian plate (e.g., Kato, 2003; Jin and Park, 2006; Schellart and Rawlinson, 2010). The deformation rates and directions of movement observed at all of the Korean GPS stations are highly similar, implying that the Korean Peninsula is located on a relatively rigid plate and is a tectonically stable region (Jin and Park, 2006).

Since 1978, more than 3000 events of small to moderate ($M < 6$) seismic magnitude have been recorded on the Korean Peninsula (Fig. 1b; KMA, 2021). The largest instrumental event (M_w 5.5) occurred in 2016 at Gyeongju City, along the YF (Figs 1b and 2a), although no earthquake-related surface rupture was reported. Kim et al. (2017b) interpreted the causative fault to be an N28°E-striking subsidiary linking fault, oblique to the main trace of the YF, on

the basis of the distribution of aftershocks and mappable faults.

Historical seismic phenomena on the Korean Peninsula, including surface rupture, tsunamis, mass movement, ground shaking, and liquefaction, as well as associated casualties and resultant damage to buildings, have been documented since CE (Common Era) 2 (Fig. 1c; Kyung, 2011). A compilation of the epicenters and intensities for the historical seismicity (Kyung, 2011) shows that there have been 10 significant earthquakes (intensity IX), of which four were located in or around Gyeongju City (Fig. S1). However, there is no clear information on the locations of causative faults for these historical earthquakes.

2.2. Yangsan Fault

The YF is one of the longest faults in SE Korea and strikes NNE–SSW with a length of ~200 km on land (Fig. 2a; e.g., Chang and Chang, 1998; Cheon et al., 2019, 2020b). On the basis of offsets of Cretaceous sedimentary rocks and (~50 Ma) Paleogene A-type granite, the YF has been identified as a dextral strike-slip fault with a cumulative horizontal displacement of 20–35 km (Fig. 2a; Chang et al., 1990; Hwang et al., 2007a, 2007b). The fault has evolved as a crustal-scale mature fault that has undergone multiple episodes of movement and deformation owing to long-term variation in the regional tectonic stress field since the Late Cretaceous and was particularly active as a dextral strike-slip fault during the late Paleogene (Cheon et al., 2019). Hence, the internal fault deformation zone (fault core and damage zone) can be as wide as hundreds of meters, although it is variable along the fault strike. Several models have been proposed regarding the segmentation of the YF based on fault geometry, kinematics, and seismic activity (e.g., Lee and Jin, 1991; Chang and Chang, 2009; Choi et al., 2017). However, the segmentation models have not been assessed with respect to paleoseismological evidence. In this study, we divided the fault into two major parts, the NYF and SYF, which connect at the junction between the YF and the Ulsan Fault (UF; Fig. 2a).

Paleoseismological studies of the YF have been conducted since the 1990s (e.g., Okada et al., 1994; Kyung et al., 1999a, 1999b; Kyung, 2003; Choi et al., 2012b; Lee et al., 2015; Kim et al., 2016; Cheon et al., 2020a; Song et al., 2020). Those studies focused mainly on investigating the existence of specific fault strand locations and stratigraphic features in trench walls. Optically stimulated luminescence (OSL) ages of the deformed layers in some of these trenches indicate that some sections of the YF have likely undergone surface rupturing during the late Quaternary (Lee et al., 2015; Cheon et al., 2020a; Song et al., 2020). However, further paleoseismological characteristics, such as earthquake timing and fault segmentation, remain lacking. Several studies have examined the Quaternary slip rate of some sections of the SYF. Kim et al. (2020) reported ~20 m horizontal geomorphic offset of young river terraces (T1–T2) along the central part of the SYF using high-resolution digital elevation models (DEMs) generated from light detection and ranging (LiDAR) and aerial photography. Kim and Seong (2021) proposed a horizontal slip rate of 1.6 ± 2.0 mm/yr by combining measurements of geomorphic offsets (130–160 m) and OSL ages (~80 ka) for river terraces in the Wolsan area (Fig. 2a).

2.3. Previous investigation of the Inbo trench site

Cheon et al. (2020a) reported surface-rupturing paleoearthquakes in trenches located in the Inbo (IB) area along the northern SYF (Fig. 2a). The IB trench was ~8 m deep and ~20 m long and provided the following observations: (1) The fault cuts unconsolidated sediments with ~7.5 m of vertical offset; (2) at least two (maybe four) surface-rupturing events can be interpreted from stratigraphic evidence; and (3) the penultimate earthquake (PE) is constrained to have occurred between 70 and 29 ka, whereas the most recent earthquake (MRE) is constrained to have postdated 29 ka on the basis of the OSL ages of sediments.

3. Methods

3.1. Fault tracing and trench locations

The northern SYF is characterized by a relatively narrow incised valley formed by differential erosion along the weak fault zone (Fig. 2b). Much of the valley floor is covered by recent sediments and is commonly urbanized. To evidence surface rupture along the northern SYF, we extracted geomorphic markers using 1:10,000 scale aerial photographs from 1954 and high-resolution DEM data (with a resolution of 0.5 m/pixel) derived from 2017 airborne LiDAR. Three trench locations were selected to the north of the I3 trench site by considering geomorphic markers and detailed field data, namely, the Wolsan (WS), Miho (MH), and Inbo north (IBN) locations. At the MH location, we conducted drilling boreholes at three sites across the inferred fault trace to identify the exact fault location and to design the depth, length, and width of the trench.

3.2. Trench excavation

We designed trenches measuring 10 to 20 m in length and 3 to 5 m in width and oriented perpendicular to subperpendicular to the NNE–SSW-striking fault trace. For detailed mapping of trench walls, we installed grids measuring 1 m × 1 m using nylon string. Trench walls were photographed using a digital camera and an unmanned aerial vehicle (*DJI Phantom 4 Pro and Mavic 2 Pro*). Commercial software (*Agisoft Metashape*) was used to produce orthogonal images of trench walls using the structure-from-motion method (Bemis et al., 2014; Johnson et al., 2014). We mapped trench walls to classify the young unconsolidated strata on the basis of their sedimentological facies and textural properties, such as grain size, matrix-to-grain ratio, compactness, roundness, sorting, and color. Unconsolidated deposits were classified into several units and subunits. Relative ages and inferred paleo-environments of formation were also considered. We also described structural features (distribution, geometry, and kinematics)

of fault splays cutting the young sediments.

3.3. Geochronology

To constrain the timing of seismic events and sediments in trenches, we collected seven OSL samples from the three trenches (WS, MH, and IBN). We also included previous OSL age dating results from the IB site (fig. 5b of Cheon et al., 2020a; personal communication with Lee, T.-H) to accurately identify the PE event in the Inbo area. For all samples, coarse-grained (25–90 μm) particles were separated by wet sieving and then treated with 10% HCL (for 3 h), 33% H_2O_2 (for 1 h), and 48% HF (for 40 min) to remove carbonates, organic materials, and feldspar grains, respectively. After acid treatment, infrared stimulated luminescence (IRSL) measurements were conducted to examine any feldspar contamination (Duller, 2003).

The OSL intensities and dose rates of all samples were analyzed using a Risø TL/OSL automatic reader (TL/OSL-DA-20) and gamma-ray spectrometer system (*Broad Energy Germanium Detector, BE 6530*) installed at the Korea Institute of Geoscience and Mineral Resources (KIGAM), Daejeon, South Korea. Equivalent dose (D_e) values were measured using the single aliquot regeneration (SAR) protocol (Murray and Wintle, 2000, 2003) with a preheat of 220 °C for 10 s and a cut-heat of 160 °C for 0 s by the preheat plateau test. Before D_e analysis, dose-recovery tests were performed to examine the adequacy of the SAR protocol. All samples show dose-recovery ratios within ±10%. The results of OSL age dating are expressed as the central age ± 1σ (1 standard error; Table 1).

At the MH site, we also collected nine charcoal samples for radiocarbon dating to calculate independent ages that could be compared and analyzed separately from the OSL ages (Table 2). Samples were repeatedly washed with an ultrasonic cleaner, following which secondary contaminants were chemically removed by acid–alkali–acid treatment. ^{14}C ages were measured with respect to standard samples at the 1MV AMS facility at the KIGAM, South Korea, and

Beta Analytic testing laboratory, USA. ^{14}C ages were calculated using Libby's half-life (5568 years) and converted to calendar dates using the IntCal20 (Reimer et al., 2020) and the OxCal (version 4.4) calibration program (https://c14.arch.ox.ac.uk/oxcal.html).

4. Results

4.1. WS trench

The WS trench is located along a narrowly incised valley whose configuration is controlled by the main strand of the YF in the Wolsan area. The geology on opposing sides of the fault is very different and the drainage network is strongly affected by the fault (Fig. 3a). More specifically, abrupt changes in the channel direction of gullies crossing the valley to become, at least for some distance, parallel to the fault strike, can be recognized. The deflected gullies show mostly right-lateral deflections, in agreement with the fault kinematics. However, these geomorphic markers can be used only to locate the actual fault trace, as it is difficult to find some consistency in the amount of offset that could be tied to a specific river terrace. In addition, in some places, deflections seem to be left-lateral, emphasizing the geomorphic control of the fault on channel morphology, but preventing any further quantitative assessment of the displacement. We attribute our geomorphic observations to the morphological expression of differential erosion between the fault zone and surrounding zones. Even though our choice of trench location was limited because of the highway at the top of the fault escarpment, we selected a trench site based on field observations, eventually excavating an E–W-oriented trench (15 m long × 2 m wide × 2.5 m deep) across the lineament in the Wolsan area (Fig. 3e). The units observed in the trench wall comprise five unconsolidated sedimentary layers overlying Cretaceous sandstone and fault rocks (Fig. 4). The block to the east ("eastern block") of the fault consists mainly of Cretaceous fine sandstone with minor ENE-dipping faults and shear fractures. The unconsolidated strata below artificial fill can be divided into

units 1 to 4 from top to bottom (see the legend of Fig. 4 for descriptions of each sedimentary layer). Units 1, 2, and 3 are found only to the west of the fault, whereas unit 4 is observed only along the eastern side. It is noted that unit 1, which is composed of poorly sorted angular to subangular pebbles and cobbles with no stratification, shows a subvertical wedge-shaped downward-tapering narrow geometry along the fault splays.

Two east-dipping fault splays with dips of >70° are developed along the eastern margin of the fault rock and cut the entire column of unconsolidated sediments except for the uppermost artificial layer. The thickness of unconsolidated sediments on top of the fractured basement differs substantially on opposing sides of the fault zone. We found that the depth to the unconformity between basement rock (eastern sandstone and western old fault rock) and overlying unconsolidated sediments is ~1.5 m higher to the east of each of the two faults relative to the west.

At this trench site, we interpret unit 1 as a key unit for characterizing earthquake history. The elongated vertical shape of unit 1, together with the nature of the in-fill clastic materials, strongly suggests that unit 1 corresponds to a fissure fill related to paleoearthquake surface rupture at this site. One fault splay is capped by unit 1, whereas the other fault splay cuts through unit 1. These features indicate that unit 1 was formed by a previous surface rupture event and was subsequently deformed by later surface rupture (Fig. 4c). The OSL ages of units 1 and 2 are 33 ± 2 and 37 ± 2 ka, respectively (Table 1). Therefore, the age of the PE event that formed unit 1 can be constrained to between 37 ± 2 and 33 ± 2 ka. The MRE event that cut unit 1 occurred after 33 ± 2 ka.

4.2. MH trench

The MH site is located ~5 km south of the WS site along the NNE–SSW-trending linear fault valley. The morphologies of opposing sides of the SYF are distinct, with a steep hillside

to the west and lower topography to the east. This difference likely reflects contrasting rock weathering properties between the volcanic rock to the west and sedimentary rock to the east (Fig. 5a). Disturbed drainage and a subtle scarp (scarplet) can be observed on the aerial images acquired in 1954, before construction of the highway (Fig. 5c and d). Significant anthropic modification of the landscape for agricultural purposes, already by 1954, prevents quantifying with certainty any horizontal offset at that site. The vertical scarplet, however, attests to the location of the fault and its probable surface-rupturing earthquake activity. Most geomorphic evidence has unfortunately been destroyed by recent construction work. A trench site was selected along the trace of the scarplet in the southern part of the Miho area, in the immediate vicinity of drainage that crosses the fault trace and which would be a possible source of fine sediments (Fig. 5e). Before excavation, we conducted drilling boreholes across the inferred fault trace to design trench size and to constrain the exact location of the most recent fault splay within a wide (tens of meters) fault core. The basement rock in the western borehole (BH-MH-01) and in the central borehole (BH-MH-02) is Cretaceous dacitic welded tuff, which is detected up to 4 m below the unconformity. In contrast, the basement rock in the eastern borehole (BH-MH-03) is composed mainly of fault rocks up to 2 m below the unconformity (Fig. 5f). On the basis of these observations, we excavated a trench between the locations of boreholes BH-MH-02 and BH-MH-03. The trench was designed with dimensions of 16 m × 6 m × 4 m and a strike of N70°W (Fig. 5f).

Figure 6 shows detailed trench logs of trench MH. The lithology in the trench wall consists of four unconsolidated units and underlying basement rocks (Cretaceous volcanic rock and fault rock derived from Cretaceous sedimentary rock). The basement of the eastern block comprises a mature fault core consisting of fault gouge, breccia, and enclosed host-rock lenses, which are derived mainly from Cretaceous sedimentary rock. In contrast, the basement of the western block is Cretaceous dacitic welded tuff. Overlying unconsolidated sediments can be

divided into units 1 to 4 from top to bottom (see the legend of Fig. 6 for descriptions of each sedimentary layer). Units 3 and 4 are observed only in the western block (footwall) of the fault, whereas units 1 and 2 overlie both the hangingwall and footwall. Unit 2 is not cut by the fault, but the observed soft-sediment deformation structures, such as flame structures and load casts, might have developed as a result of strong shaking (Fig. 6c). Unit 3N of the northern wall consists mostly of poorly sorted, subangular gravel beds in the lower part and fine grayish sand to clay with some pebbles in the upper part, and is cut by the main fault splay. The unit shows a wedge-shaped geometry that widens toward the fault splay, and the grain size coarsens toward the fault splay in the trench wall. Unit 3S of the southern wall displays a U-shaped cut-and-fill geometry and comprises mostly subangular to subrounded pebbles to cobbles, although this unit has similar clast compositions to those of unit 3N in the northern wall.

In the MH trench wall, a fault splay is developed along the western margin of the mature fault core, which affects units 3 and 4 and is covered by unit 2.3. The fault splay strikes NNE–SSW and dips toward the ESE at an angle of >70°. The vertical offset between units across the fault is ~1.5 m, as assessed from the differing position of the unconformity between unconsolidated strata and basement rocks. On the basis of relative cross-cutting relationships between the fault and the different sedimentary units, we propose that the MRE occurred after the deposition of unit 3 and before deposition of unit 2.3. However, unit 3N of the northern wall has a wedge-shaped geometry and consists mainly of poorly sorted gravels showing upward fining and faultward coarsening. The sedimentary facies imply that the unit was rapidly deposited as a result of an abrupt surface process associated with a surface-rupturing event. These features imply that unit 3 was probably formed by a previous surface rupture and was subsequently cut by a later surface rupture.

Depositional ages inferred from radiocarbon dating of units 2.2 and 3 are presented in Table 2 and Figure 6. Six samples from unit 2.2 yield consistent ages of ~15,000 cal yr BP and

three samples from unit 3 yield ages of ~28,000 cal yr BP. We calibrated their conventional radiocarbon ages and calculated each weighted mean using OxCal4.4 (Table 2; Ramsey, 2009, 2017). In contrast, the OSL ages of units 2.3 and 3 are 30 ± 1 and 35 ± 2 ka, respectively (Table 1). The OSL ages of the MH trench are thus systematically older than the radiocarbon ages. The consistency of the radiocarbon ages for each unit advocates for their high reliability. However, we also note that the OSL dating is characterized by a high-quality measurement of the OSL signal for the following reasons: (1) a feldspar/quartz ratio of <1% was achieved; (2) a measured/given ratio (dose-recovery test) of >90% in the pre-screening test performed before the estimation of De was achieved (Fig. S2); and (3) the level of sensitivity of the OSL signal, decay curve, growth curve, and probability density plot identified by the normal distribution of aliquots was satisfactory (Fig. S3). Our best explanation of the different ages between ^{14}C and OSL is that the older ages for OSL are related to incomplete bleaching of sediments owing to a combination of river turbidity, short sediment transport distance, and abrupt emplacement. Therefore, in our interpretations, we consider that the radiocarbon ages are syn to minimum depositional ages and that the OSL ages are maximum depositional ages. At the MH site, we regard the boundary between units 2 and 3 as a possible event horizon, constraining the timing of the MRE to 28,000–15,000 cal yr BP using radiocarbon dating. When considering the OSL ages, the age range of the MRE could be older (35 ± 2 ka).

4.3. IBN trench

The IBN trench is located along the eastern branch of the main SYF (Figs 2 and 7), ~500 m north of the IB trench (Cheon et al., 2020a). The fault trace cross-cuts alluvial fans derived from the eastern hills formed by Cretaceous sedimentary rocks (Fig. 7a and b). A small westward-flowing gully and alluvial fans show right-lateral deflection (Fig. 7c). Borehole investigation has revealed that the unconformity depth shows an abrupt gap between the eastern

and western blocks across the fault splay (Cheon et al., 2020a). The IBN trench location was selected to maximize the chances of uncovering fine overbank sediments rather than coarser alluvial-fan deposits. The trench strikes N70°W, subperpendicular to the lineament, and has dimensions of 18 m × 3 m × 3 m (Fig. 7d).

Figure 8 shows detailed trench logs of the IBN trench. The lithology of the trench is composed primarily of three unconsolidated sedimentary units overlying basement rock (see the legend of Figure 8 for descriptions of each sedimentary layer). The eastern basement comprises severely damaged Cretaceous sedimentary rock with fault gouge and breccia. Unfortunately, we were unable to reach the basement of the western block in the trench wall. The overlying unconsolidated deposits are grouped into units 1 to 3 from top to bottom. This sequence is covered by a ~1-m-thick layer of artificial landfill. We recognized the capping layer (unit 1) that seals the fault, whereas units 2 and 3 are displaced by the fault. Unit 3 appears to be thrusted by the older basement rock. In addition, unit 3.2 shows a drag pattern close to the fault splay, consistent with a reverse sense of movement. Gouge foliations along the fault splay and striations on slip surfaces indicate a dextral sense of slip.

We collected OSL samples from units 1.2 and 2 to determine the timing of faulting within the IBN trench. Unit 1.2 is the oldest layer that is undeformed by faulting, and unit 2 is the uppermost layer that is cut by the fault. The OSL ages of units 1.2 and 2 are 17 ± 1 and 37 ± 2 ka, respectively (Table 1). On the basis of the presence of the earthquake horizon between units 1.2 and 2 and the OSL ages of these units, we constrain the age of the MRE at 37 ± 2 to 17 ± 1 ka. At the IB trench site, 500 m south of the IBN trench, the MRE event is inferred to have occurred after 29 ± 1 ka (Cheon et al., 2020a). In this study, we regard the IBN and IB trenches as having the same slip behavior because the two sites are spatially close (~500 m) on the same straight fault line without any discontinuity. Combined with previous findings and our new results, the age of the MRE of the IBN and IB trenches can be constrained to between 29 ± 1

and 17 ± 1 ka. We also obtained an additional OSL age of 52 ± 3 ka from unit 1.3 in the IB trench (Table 1; fig. 5b in Cheon et al., 2020a; personal communications with Lee, T.-H), and this unit overlies the PE rupture. Our OSL age helps to constrain the timing of the PE in the IB trench as 70 ± 4 to 52 ± 3 ka.

5. Discussion

5.1. Earthquake kinematics inferred from stratigraphic features

In general, surface rupture within a strike-slip fault zone shows complex deformation involving not only a strike-slip component but also a dip-slip component and/or folding. For example, the Little River Fault in the USA, which generated a 3-km-long surface rupture during the Sparta earthquake (M_w 5.1, 2020), showed left-lateral slip, but low-angle thrust faults are observed at the surface (Figueiredo et al., 2022). Recent morphotectonic studies using airborne LiDAR data have shown that the YF has undergone dominantly dextral slip with minor reverse slip (e.g., Cheon et al., 2020a; Kim et al., 2020; Song et al., 2020). In this section, we raise the issue of the tendency of previous excavation surveys along the YF to focus only on the minor reverse component owing to limited 2D observations in trench walls. In fact, in some cases, the apparent vertical displacement was determined by measuring the height or vertical separation of layers that had been slipped laterally. Here, we deal with stratigraphic features associated with surface depositional processes related to strike-slip earthquakes with a secondary component of compression.

Our observations of stratigraphic features in trench walls indicate that fault scarps are closely associated with horizontal slip. In the WS trench, unit 1 shows a downward-tapering geometry along the subvertical fault splay and consists of poorly sorted, angular to subangular gravels. Although fissures are observed in a variety of structural settings (McCalpin et al., 2009), we propose that the near-vertical void space could have been formed by a surface rupture

event with strike-slip-related faulting on the basis of the general kinematics of the fault splay and the distribution, geometry, and sedimentological features of the fissure (Fig. 9a; Wright et al., 2009). In the northern wall of the MH trench, we identified a westward-tapering colluvial wedge deposit showing coarsening of subangular clasts with decreasing distance from the fault (unit 3N). The unit probably evolved as a local sag pond owing to minor damming-up of streamflow (Fig. 9b). It is noted that the colluvial wedge and damming-up streamflow could be indicators of a reverse component. In the southern wall of the MH trench, however, the corresponding layer, unit 3S, shows a cut-and-fill geometry, implying channel deposits. This signifies the development of a small gully along the rupture traces with the formation of the sag pond. Variation in topographic features over a short distance (a trench width of several meters) is one of the typical markers of horizontally displaced undulating relief (Fig. 9c).

The studied section of the SYF has acted as a dextral slip fault with only a small reverse component during the imposed under the current stress regime. However, in naturally exposed outcrops or trench walls, the reverse component appears to be highlighted because of exposure and trench geometry. To understand the kinematics of a fault splay, both topographic analysis and trench surveys should be conducted. Our study has shown that even for a strike-slip-dominant fault such as the YF, detailed sedimentological analysis can provide useful information regarding rupture kinematics. We argue that in the absence of geomorphic evidence of earthquake surface ruptures, stratigraphic features can be indirect indicators of earthquake kinematics.

5.2. Spatiotemporal paleoseismological behavior of the Yangsan Fault

5.2.1. Rupture scenarios for the southern Yangsan Fault

In general, owing to low rates of deformation and long earthquake recurrence intervals, sparse paleoseismological data make it more difficult to build rupture scenario for intraplate

fault systems. Determination of rupture scenarios is beset by various complexities, including spatial biases in the distribution of study sites along a fault, difficulty in correlating layers from one site to the other, and uncertainties associated with ages measured using different dating methods (e.g., OSL, ^{14}C, or cosmogenic nuclides). Because of these limitations, paleoseismologists tend to present a range of alternative scenarios consistent with the available paleoseismological data (DuRoss et al., 2016). In the present study, we propose two possible rupture scenarios based on the chronology of each paleosurface rupture at four trench sites.

We compiled paleoseismological data from three new trenches (the WS, MH, and IBN trenches) and one previously excavated trench (the IB trench; Cheon et al., 2020a), all of which are located along a 10-km-long section of the southern YF. Figure 10 shows possible rupture models based on rupture timing within the study area. In the WS trench, we recognized at least two surface rupture events. The PE event forming a narrow fissure along the fault splay occurred during 37 ± 2 to 33 ± 2 ka, following which the fissure-filling deposit was offset by reactivation of the fault splay during the MRE event (Fig. 4c; after 33 ± 2 ka). In the MH trench wall, we observed only one fault splay that transected the unconsolidated layers. This deformation could have resulted from one rupturing event, but the sedimentary characteristics of unit 3, such as grain size, sorting, and roundness of pebbles, indicate that the rapid sedimentation of this unit is associated with the fault-related morphology. Therefore, this fault may have slipped twice after the deposition of unit 4. Units 3 and 4 were cut by the MRE event of 28,000 (or 35 ± 2 ka considering the OSL age) to 15,000 cal yr BP. If unit 3 developed immediately after surface rupture, the PE could have occurred before 28,000 cal yr BP. At the IBN trench site, we recognized only one paleoearthquake. We constrained the timing of the MRE there from 37 ± 2 to 17 ± 1 ka on the basis of measured OLS ages of the earthquake horizon between units 1.2 and 2. At the IB trench site, 500 m south of the IBN trench site, the MRE event occurred after 29 ± 1 ka, as estimated using the OSL age of 29 ± 1 ka (Cheon et

al., 2020a). As mentioned above, we regard the IBN and IB trenches as having the same earthquake history. Integration of previous findings with our new results yields an age for the MRE at the IBN and IB trench sites of 29 ± 1 to 17 ± 1 ka. We also combined the OSL age of 52 ± 3 ka from unit 1.3 in the IB trench (Cheon et al., 2020a), which overlies the PE rupture, with our new OSL age to constrain the timing of the PE in the IB trench as 70 ± 4 to 52 ± 3 ka.

The correlation of paleoseismological data between different trench sites suggests that the MRE might have ruptured the entire studied fault section at ~28,000 cal yr BP (or 30 ± 1 to 17 ± 1 ka when considering the OSL age). However, we are unable to completely rule out the possibility that our observations for the MRE correspond to cumulative deformation associated with several events over periods of tens to thousands of years, although the sedimentological observations in trenches do not support this option. Regarding the pre-MRE events, we suggest two possible scenarios. The first scenario is that the whole studied section slipped over its total length twice, during 70 ± 4 to 52 ± 3 ka and 37 ± 2 to 33 ± 2 ka (Fig. 10c). In this scenario, however, we need to assume that we could not recognize one or more events at each trench site, possibly owing to obliteration of evidence by surface processes during inter-seismic periods. The scenario implies the occurrence of at least three earthquake events in each trench, although the three ruptures could not be seen together in any of the studied trenches. The second scenario involves a partial rupturing model (Fig. 10d). We recognized two earthquakes at each trench site (except for the single event detected at the IBN site, which was combined with the observations at the IB site; see Section 4.3). The PE of the WS–MH and IBN–IB sections occurred at 37 ± 2 to 33 ± 2 ka and at 70 ± 4 to 52 ± 3 ka, respectively. According to this scenario, the WS-MH and IBN-IB sections either slipped separately or together (at MRE) depending on the event (Fig. 10d).

The second of these scenarios is regarded as more plausible, as it involves fewer assumptions. We also note that there are geomorphic and geological differences between the

WS–MH and IBN–IB sections that could control their slip behavior: (1) The WS–MH section is located along a narrow fault valley, whereas the IBN–IB section is located along the eastern part of a wide fault valley (Fig. 2b); and (2) paleoseismological faults bound the main fault core zone at the WS and MH sites, whereas those at the IBN and IB sites have slipped along the eastern branch fault of the YF, with the branching point being situated between the MH and IBN sites (Fig 10a; Lee et al., 2020). In map view, the main strand of the YF bends slightly right by ~7° at the branching point. Therefore, we infer that the recent rupture behaviors are associated with the distinct structural patterns of the fault in different sections. We further discuss the fault geometry effect and its dependence on scale in Section 5.2.2.

5.2.2. Correlation of earthquake timings for the entire Yangsan Fault during the late Quaternary

Although the YF can be easily traced for ~200 km on land, many parts of the fault have not been investigated because the fault passes through urbanized or agricultural areas. For this reason, only a few sites have yielded estimates of paleoseismological timing. Here, we comprehensively compare MRE timings of previous studies with our results to better understand the recent fault activity of the YF. We summarize the MRE timings along the YF and UF in Figure 11 and Table S1. Sites Y01–Y03 along the NYF are the most-studied sites of the entire YF with respect to paleoseismology (Fig. 11; Kyung, 2003; Lee et al., 2015; Cho et al., 2016; Song et al., 2020). The ages of the MRE events at the Y01–Y03 sites have been estimated as ≤2.7–1.3 ka (Kyung, 2003) and ≤3.2 ka (Song et al., 2020), respectively. In addition, several sites along the UF have recorded stratigraphic evidence of paleoearthquakes during the Holocene (e.g., Okada et al., 1999; Inoue and Choi, 2006; Kyung, 2010; Choi et al., 2012b; Kim et al., 2021). At the IBN and MH sites, Late Pleistocene strata overlie the paleo-surface ruptures and have not been deformed. These features suggest that along the studied

section the most recent event predate the Holocene. Therefore, the ages of the MRE in our studied section of the SYF are likely older than those of the NYF and UF. However, other possibilities cannot be discounted, such as that evidence of Holocene surface ruptures may not have been identified owing to the particular locations of our excavation sites.

Although our review of results (summarized in Fig. 11) does not point unambiguously toward coseismic ruptures, these results suggest that the two studied sections of the SYF have undergone different seismic histories during the current tectonic regime. Furthermore, the boundary between the NYF and SYF, where the strike of the YF changes, also corresponds to the junction between the YF and the UF. Our comprehensive investigation has revealed that the NYF and SYF have distinct paleoseismological histories, and we infer that the interconnection of the YF with the UF has acted as an important structural break-point separating different seismic behaviors along the YF system.

In general, rupture behavior is influenced by geometrical variations in fault structure, such as bending or jog configuration (e.g., branch and fault splays), and by interconnections with other faults (Wesnousky, 2008; Biasi and Wesnousky, 2016, 2017; Vallage et al., 2016; Choi et al., 2018). In particular, large adjacent structures can strongly influence fault-slip behavior and seismicity (Klinger et al., 2017). Studies of the Futagawa–Hinagu fault zone (2016 Kumamoto earthquake; Manjo et al., 2019), the central Denali and Totschunda faults (2002 Denali earthquake; Dreger et al., 2004; Haeussler et al., 2004; Schwartz et al., 2012), the Kusai segment of the Kunlun Fault and the Kunlun Pass Fault (2001 Kunlun earthquake; Vallée et al., 2008; Klinger et al., 2017), and the Bulnay Fault (1905 Bulnay-Tsetserleg earthquake; Choi et al., 2018) have revealed that rupture propagation is controlled by obliquely to subparallelly striking faults rather than straight structures. Although these published cases and our studied sections involve different temporal scales, fault geometry could have similarly affected rupture behavior.

Our comprehensive data show no record of surface-rupturing earthquakes during the Holocene, at least in the studied section of the SYF. However, Korean historical literature documents a number of hazardous earthquakes around Gyeongju City, in the junction area between the YF and UF (Fig. S1; Kyung et al., 2011). The historical seismicity cases in Figure S1 caused numerous casualties and damage in Gyeongju City, but there are no geologic records that correlate with the documented damaging earthquakes. We propose two options for the origin of this historical seismicity. First, if these earthquakes originated from the SYF but were only moderate in size, then they might not have generated surface ruptures. This idea is supported by the fact that historical earthquakes near Gyeongju City do not seem to have large magnitudes, as there are no reports of these shocks in adjacent areas. Similarly, the 2016 Gyeongju Earthquake (M_w 5.5) caused severe damage to buildings, roads, and other structures, but no surface ruptures were reported (Kim et al., 2017b). Alternately, earthquakes could have been located in neighboring areas along the NYF and/or UF. However, paleoseismological evidence for historic earthquakes along the NYF and UF would be needed to test this possibility.

6. Conclusions

We conducted detailed geomorphic analyses and paleoseismological trench surveys at three sites (WS, MH, and IBN) and numerical age dating (OSL and ^{14}C) of unconsolidated sediments along the northern section of the SYF in SE Korea to characterize the spatiotemporal distribution of Late Pleistocene surface ruptures. Combining our results with previous findings for the IB trench allows the following conclusions to be drawn.

1. The kinematics of the paleoseismological fault splays causing surface ruptures show dextral slip with a small reverse component, expressed in the field as east-side-up geometry along eastward-dipping fault splays and dextrally offset streams and terraces. Stratigraphic features related to fault kinematics include fissure-filling deposits, sag

ponds, and U-shaped cut-and-fill stream deposits along fault splays in two-dimensional trench walls. In general, these types of stratigraphic features along the fault can provide useful information regarding strike-slip rupture kinematics in intraplate regions, where geomorphic expressions of surface ruptures are limited.

2. We suggest two possible rupture scenarios of the timing of the MRE and PE along the studied section: (1) Considering the possibility of a missing event in trench walls, three full-rupturing earthquakes occurred along the entire studied section at 70 ± 4 to 52 ± 3 ka, 37 ± 2 to 33 ± 2 ka, and after 28,000 cal yr BP (or 30 ± 1 to 17 ± 1 ka considering the OSL age); or (2) before the full-rupturing earthquake along the whole studied section at the timing of the MRE, partial ruptures occurred along the IBN–IB section during 70 ± 4 to 52 ± 3 ka and the WS–MH section during 37 ± 2 to 33 ± 2 ka. Each rupture scenario suggests different fault-slip models, which could affect the seismic hazard assessment field.
3. According to the full-rupture scenario, each rupture length within a given fault section might be constant, as in the characteristic earthquake model, but this scenario requires many assumptions. In contrast, in the partial rupture scenario, parts of the studied section slip either separately or together, such as in the uniform slip model, which is the favored model for our data. Fault geometry showing a right bend of ~7° of the main SYF at the junction with the eastern branch of the YF, which is located between the MH and IBN sites, could influence the slip behavior of different sections of the SYF.
4. The MRE of the NYF and UF is presumed to have occurred during the Holocene, whereas that of the SYF occurred pre-Holocene. The boundary between the NYF and SYF is an area where the UF terminates by curving into the YF, at which point the general strike of the YF changes. Our findings suggest that the distinct rupture

histories of different sections of the YF could be controlled by the large-scale branching geometry of the fault system.

Acknowledgments

This research was supported by a grant (GP2020-014) from the Research in Active Tectonics and Development of a Fault Segmentation Model for Intraplate Regions from the Basic Research Project of the Korea Institute of Geoscience and Mineral Resources funded by the Korean Ministry of Science and ICT (South Korea).

References

Back, J.J., Kyung, J.B., Choi, H., 2011. Analysis on the source characteristics of the recent five-year earthquakes occurred in the central and western areas of the Korean Peninsula. J. Kor. Ear. Sci. Soc. 32, 161–169 (in Korean with English abstract).

Bae, S., Jeon, S., Kim, J., Kim, J., 2008. Characteristics of the regional rock stress field at shallow depth in the Kyungsang Basin with In-situ rock stress measurements. J. Kor. Soc. Rock Mec. 18, 149–161 (in Korean with English abstract).

Bemis, S.P., Micklethwaite, S., Turner, D., James, M.R., Akciz, S., Thiele, S.T., Bangash, H.A., 2014. Ground-based and UAV-Based photogrammetry: A multi-scale, high-resolution mapping tool for structural geology and paleoseismology. J. Struct. Geol. 69, 163–178. https://doi.org/10.1016/j.jsg.2014.10.007

Berryman, K.R., Cochran, U.A., Clark, K.J., Biasi, G.P., Langridge, R.M., Villamor, P., 2012. Major Earthquakes Occur Regularly on an Isolated Plate Boundary Fault. Science. 336, 1690–1693. https://doi:10.1126/science.1218959

Biasi, G.P., Wesnousky, S.G., 2016. Steps and gaps in ground ruptures: Empirical bounds on rupture propagation. Bull. Seismol. Soc. Am. 106(3), 1110-1124. https://doi.org/10.1785/0120150175

Biasi, G.P., Wesnousky, S.G., 2017. Bends and ends of surface Ruptures. Bull. Seismol. Soc. Am. 107, 2543-2560. https://doi.org/10.1785/0120160292

Bollinger, L., Klinger, Y., Forman, S.L., Chimed, O., Bayasgalan, A., Munkhuu, U., Davaasuren, G., Dolgorsuren, T., Enkhee, B., Sodnomsambuu, D., 2021. 25,000 years long seismic cycle in a slow deforming continental region of Mongolia. Sci. Rep. 11, 17855. https://doi.org/10.1038/s41598-021-97167-w

Burbank, D.W., Anderson, R.S., 2013. Tectonic Geomorphology, second edition. Blackwell Science, Oxford.

Calais, E., Camelbeeck, T., Stein, S., Liu, M., Craig, T. J., 2016. A new paradigm for large earthquakes in stable continental plate interiors. Geophys. Res. Lett. 43, 10621− 10637. https://doi.org/10.1002/2016GL070815

Chang, C., Lee, J.B., Kang, T.-S., 2010. Interaction between regional stress state and faults: complementary analysis of borehole in situ stress and earthquake focal mechanism in southeastern Korea. Tectonophysics 485, 164–177. https://doi.org/10.1016/j.tecto.2009.12.012

Chang, C.-J., Chang, T.W., 1998. Movement History of the Yangsan Fault based on Paleostress Analysis. J. Eng. Geol. 8, 35–49 (in Korean with English abstract).

Chang, C.-J. Chang, T.W., 2009. Behavioral characteristics of the Yangsan Fault based on geometric analysis of fault slip. J. Eng. Geol. 19, 277–285 (in Korean with English abstract).

Chang, K.H., Woo, B.G., Lee, J.H., Park, S.O., Yao, A., 1990. Cretaceous and Early Cenozoic stratigraphy and history of eastern Kyongsang Basin, S. Korea. J. Geol. Soc. Korea 26, 471–487.

Cheon, Y., Cho, H., Ha, S., Kang, H., Kim, J.-S., Son, M., 2019. Tectonically controlled multiple deformations along the Yangsan Fault Zone, SE Korea, since Late Cretaceous. J. Asi. Ear. Sci. 170, 188–207. https://doi.org/10.1016/j.jseaes.2018.11.003

Cheon, Y., Choi, J.-H., Choi, Y., Bae, H., Han, K.-H., Son, M., Choi, S.-J., Ryoo, C.-R., 2020b. Understanding the distribution and internal structure of the main core of the

Yangsan Fault Zone: Current trends and future work. J. Geol. Soc. Korea 56, 619–640 (in Korean with English abstract).

Cheon, Y., Choi, J.-H., Kim, N., Lee, H., Choi, I., Bae, H., Rockwell, T.K., Lee, S.R., Ryoo, C.-R., Choi, H., Lee, T.-H., 2020a. Late Quaternary transpressional earthquakes on a long-lived intraplate fault: A case study of the Southern Yangsan Fault, SE Korea. Quat. Int. 553, 132–143. https://doi.org/10.1016/j.quaint.2020.07.025

Cho, S.-I., Choi, W.-H., Inoue, D., Kim, Y.-S., 2016. Geological evolution of active fault at Dangu-ri, Gyeong-ju area, SE Korea. 7th International INQUA Meeting on Paleoseismology, Active Tectonics and Archeoseismology (PATA), 30 May to 3 June, 2016, Crestone, Colorado, USA.

Choi, H., Hong, T.-K., He, X., Baag, C.-E. 2012a. Seismic evidence for reverse activation of a paleo-rifting system in the East Sea (Sea of Japan). Tectonophysics, 572–573, 123–133. https://doi.org/10.1016/j.tecto.2011.12.023

Choi, J.-H., Kim, Y.-S., Klinger, Y., 2017. Recent progress in studies on the characteristics of surface rupture associated with large earthquakes. J. Geol. Soc. Korea 53(1), 129-157 (in Korean with English abstract).

Choi, J.-H., Klinger, Y., Ferry, M., Ritz, J.-F., Kurtz, R., Rizza, M., Bollinger, L., Davaasambuu, B., Tsend-Ayush, N., Demberel, S, 2018. Geologic Inheritance and Earthquake Rupture Processes: The 1905 M≥8 Tsetserleg-Bulnay Strike-Slip Earthquake Sequence, Mongolia. J. Geophys. Res. Solid Earth 123, 1925–1953. https://doi.org/10.1002/2017JB013962

Choi, S.J., Jeon, J.S., Song, K.Y., Kim, H.C., Kim, Y.H., Choi, P.Y., Choi, W.C., Han, J.G., Ryoo, C.R., Sun, C.G., Jun, M.S., Kim, G.Y., Kim, Y.B., Lee, H.J., Shin, J.S., Lee, Y.S., Gi,

W.S., Lee, H.K., Song, Y.G., Kim, Y.S., Kang, T.S., Hong, D.G., Kim, S.K., 2012b. Active Fault Map and Seismic Hazard Map. Natural Hazards Mitigation Research Group, National Emergency Management Agency.

Chough, S.K., Sohn, Y.K., 2010. Tectonic and sedimentary evolution of a Cretaceous continental arc–backarc system in the Korean peninsula: New view. Ear.-Sci. Rev. 101(3), 225–249. https://doi.org/10.1016/j.earscirev.2010.05.004

DeMets, C., Gordon, R.G., Argus, D.F., Stein, S., 1994. Effect of recent revisions to the geomagnetic reversal time scale on estimates of current plate motions. Geophys. Res. Lett. 21, 2191–2194. https://doi.org/10.1029/94GL02113

Dreger, D.S., Oglesby, D.D., Harris, R., Ratchkovski, N., Hansen, R., 2004. Kinematic and dynamic rupture models of the November 3, 2002 Mw7.9 Denali, Alaska, earthquake. Geophys. Res. Lett. 31. https://doi.org/10.1029/2003GL018333

Duller, G.A.T., 2003. Distinguishing quartz and feldspar in single grain luminescence measurements. Rad. Meas. 37, 161–165. https://doi.org/10.1016/S1350-4487(02)00170-1

DuRoss, C.B., Personius, S.F., Crone, A.J., Olig, S.S., Hylland, M.D., Lund, W.R., Schwartz, D.P., 2016. Fault segmentation: New concepts from the Wasatch Fault Zone, Utah, USA, J. Geophys. Res. Solid Earth 121, 1131–1157. https://doi.org/10.1002/2015JB012519

Elliott, A.J., Oskin, M.E., Liu-zeng, J., Shao, Y.-X., 2018. Persistent rupture terminations at a restraining bend from slip rates on the eastern Altyn Tagh fault, Tectonophysics 733, 57–72. https://doi.org/10.1016/j.tecto.2018.01.004

England, P., Jackson, J., 2011. Uncharted seismic risk. Nat. Geosci. 4, 348–349. https://doi.org/10.1038/ngeo1168

Figueiredo, P., Hill, J., Merschat, A., Scheip, C., Stewart, K., Owen, L., Wooten, R., Carter, M., Szymanski, E., Horton, S., Wegmann, K., Bohnenstiehl, D., Thompson, G., Witt, A., Cattanach, B., Douglas, T., 2022. The Mw 5.1, 9 August 2020, Sparta Earthquake, North Carolina: The First Documented Seismic Surface Rupture in the Eastern United States. Geol. Soc. Am. 32, 3–4. https://doi.org/10.1130/GSATG517A.1. CC-BY-NC

Grant, L.B., Sieh, K., 1994. Paleoseismic evidence of clustered earthquakes on the San Andreas fault in the Carrizo Plain, California. J. Geophys. Res. 99(B4), 6819–6841. https://doi.org/10.1029/94JB00125

Haimson, B.C., Lee, M.Y., Song, I., 2003. Shallow hydraulic fracturing measurements in Korea support tectonic and seismic indicators of regional stress. Int. J. Roc. Mec. Min. Sci. 40, 1243–1256. https://doi.org/10.1016/S1365-1609(03)00119-9

Haeussler, P.J., Schwartz, D.P., Dawson, T.E., Stenner, H.D., Lienkaemper, J.J., Sherrod, B., Cinti, F.R., Montone, P., Craw, P.A., Crone, A.J., Personius, S.F., 2004. Surface Rupture and Slip Distribution of the Denali and Totschunda Faults in the 3 November 2002 M 7.9 Earthquake, Alaska. Bull. Seismol. Soc. Am. 94(6B), S23-S52. https://doi.org/10.1785/0120040626

Hoe, S.Y., Kyung, J.B., 2008. Fault Plane Solutions for the Recent Earthquakes in the Central Region of South Korea. J. Kor. Ear. Sci. Soc. 29, 437–445.

Hwang, B.-H., Lee, J.-D., Yang, K., McWilliams, M., 2007a. Cenozoic strike-slip displacement along the Yangsan Fault, southeast Korean Peninsula. Int. Geol. Rev., 49, 768–775. https://doi.org/10.2747/0020-6814.49.8.768

Hwang, B.-H., McWilliams, M., Son, M., Yang, K., 2007b. Tectonic implication of A-type Granites across the Yangsan Fault, Gigye and Gyeongju areas, southeast Korean Peninsula.

Int. Geol. Rev. 49, 1094–1102. https://doi.org/10.2747/0020-6814.49.12.1094

Inoue, D., Choi, W.-H., 2006. The activity of the Ulsan Fault system based on marine terrace age study at the southeastern part of Korean Peninsula. Denryoku Chuo Kenkyusho Hokoku.

Jin, S., Park, P.-H., 2006. Strain accumulation in South Korea inferred from GPS measurements. Ear. Plan. Spa. 58, 529–534. https://doi.org/10.1186/BF03351950

Johnson, K., Nissen, E., Saripalli, S., Arrowsmith, J.R., McGarey, P., Scharer K., Williams, P., Blisniuk, K., 2014. Rapid mapping of ultrafine fault zone topography with structure from motion. Geosphere 10, 969–986. https://doi.org/10.1130/GES01017.1

Kato, T., 2003. Tectonics of the eastern Asia and the western Pacific as seen by GPS observations. Geosci. J. 7, 1–8. https://doi.org/10.1007/BF02910259

Kee, W.-S., Kim, S.W. Kim, H., Hong, P., Kwon, C.W., Lee, H,-J., Cho, D.-L., Koh, H.J., Song, K.-Y., Byun, U.H., Jang, Y., Lee, B.C., 2019. Geologic Map of Korea (1:1,000,000). KIGAM.

Keller, E.A., Pinter, N, 2001. Active Tectonics, Earthquakes, Uplift, and Landscape, second edition. Prentice Hall, New Jersey.

Kim, D.-E., Seong, Y.B., 2021. Cumulative slip rate of the Southern Yangsan fault from geomorphic indicator and numerical dating. J. Kor. Geograph. Soc. 56(2), 201–213 (in Korean with English abstract).

Kim, H., Synn, J.-H., Park, C., Song, W.K., Park, E.S., Jung,Y.-B., Cheon, D.-S., Bae, S., Choi, S.-O., Chang, C., Min, K.-B., 2021. Korea stress map 2020 using hydraulic fracturing and overcoring data. Tun. Undergr. Spa. 31, 145–166 (in Korean with English

abstract).

Kim, M.-C., Jung, S., Yoon, S., Jeong, R.-Y., Song, C.W., Son, M., 2016. Neotectonic crustal deformation and current stress field in the Korean Peninsula and Their Tectonic Implications: a review. J. Petrol. Soc. Korea 25, 169–193 (in Korean with English abstract).

Kim, N., Choi, J.-H., Park, S.-I., Lee, T.-H., Choi, Y., 2020. Cumulative offset analysis of the Central-Southern Yangsan Fault based on topography of Quaternary fluvial terrace. J. Geol. Soc. Korea 56, 135–154 (in Korean with English abstract).

Kim, T., Kim, D.-E., Kim, S.-J., Seong, Y.B., Lim, H.S., Shin, H.-C., Kim, Y.-S., 2021. Kinematic characteristics and movement timing of the Wonwonsa fault in the central Ulsan fault. J. Geol. Soc. Korea 57, 35–48 (in Korean with English abstract).

Kim, T., Shin, H.-C., Kim, Y.-S., 2020. Characteristics of the topographical deformation in the central part of the Ulsan fault. J. Geol. Soc. Korea 56, 193-209 (in Korean with English abstract).

Kim, Y.H., He, W.H., Ni, S.D., Lim, H., Park, S.-C., 2017a. Earthquake Source Mechanism and Rupture Directivity of the 12 September 2016 M_w 5.5 Gyeongju, South Korea, Earthquake. Bull. Seis. Soc. Am. 107, 2525–2531. https://doi.org/10.1785/0120170004

Kim, Y.-S., Kim, T., Kyung, J.B., Cho, C.S., Choi, J.-H., Choi, C.U., 2017b. Preliminary study on rupture mechanism of the 9.12 Gyeongju Earthquake. J. Geol. Soc. Korea 53, 407–422 (in Korean with English abstract).

Klinger, Y., Choi, J. H., Vallage, A., 2017. Fault branching and long-term earthquake rupture scenario for strike-slip earthquakes. In Fault Zone Dynamic Processes: Evaluation of Fault Properties During Seismic Rupture, Geophysical Monograph 227, 217-228, edited by M.Y.

Thomas, T.M. Mitchell and H.S. Bhat, co-published by AGU and Wiley &Sons, Hoboken, USA. https://doi.org/10.1002/9781119156895.ch11

KMA(Korea Meteorological Administration)., 2021. Lists for instrumental earthquake records of Korea. Available from: http://www.weather.go.kr/weather/earthquake_volcano/domesticlist.jsp#btn_next (15 February 2021).

Ko, K., Choi, S.-J., Lee, T.-H., Gihm, Y.S., Kim, C.-M., Kim, K., Cheon, Y., 2022. A multidisciplinary approach to characterization of the mature northern Yangsan fault in Korea and its active faulting. Mar. Geophys. Res. 43, 21. https://doi.org/10.1007/s11001-022-09486-w

Kuwahara, Y., Choi, J.-H., Cheon, Y., Imanishi, K., 2021. Dependence of earthquake faulting type on fault strike across the Korean Peninsula: Evidence for weak faults and comparison with the Japanese Archipelago. Tectonophysics, 804, 228757. https://doi.org/10.1016/j.tecto.2021.228757

Kyung, J.B., 2003. Paleoseismology of the Yangsan Fault, southeastern part of the Korean Peninsula. Ann. Geophys. 46, 983–996. https://doi.org/10.4401/ag-3465

Kyung, J.B., 2010. Paleoseismological Study and Evaluation of Maximum Earthquake Magnitude along the Yangsan and Ulsan Fault Zones in the Southeastern Part of Korea. Jigu-Mulli-wa-Mulli-Tamsa, 13, 187–197 (in Korean with English abstract).

Kyung, J.B., 2011. Data base for historical earthquake records in the Korean Peninsula (III). Korea Meteorological Agency report, Seoul, 645.

Kyung, J.B., Lee, K., Okada, A., 1999a. A paleoseismological study of the Yangsan fault - analysis of deformed topography and trench survey. J. Kor. Geophys. Soc. 2, 155-168 (in

Korean with English abstract).

Kyung, J.B., Lee, K., Okada, A., Watanabe, M., Suzuki, Y., Takemura, K., 1999b. Study of fault characteristics by trench survey in the Sangchon-ri area in the southern part of Yangsan fault, southeastern Korea. J. Kor. Ear. Sci. Soc. 20, 101–110 (in Korean with English abstract).

Lee, J., Rezaei, S., Hong, Y., Choi, J.-H., Choi, J.-H., Choi, W.-H., Rhee, K.-W., Kim, Y.-S., 2015. Quaternary fault analysis through a trench investigation on the northern extension of the Yangsan fault at Dangu-ri, Gyungjusi, Gyeongsanbuk-do. J. Geol. Soc. Kor. 51, 471–485 (in Korean with English abstract).

Lee, K., Jin, Y.G., 1991. Segmentation of the Yangsan fault system: Geophysical studies on major faults in the Kyeongsang Basin. J. Geol. Soc. Kor. 27, 434–449 (in Korean with English abstract).

Lee, S.R., 39 others, 2020. Research on geologic hazard assessment of large fault system-focusing on central region of the Yangsan fault (R&D Report NP2018-017). KIGAM, Daejeon, 502p.

Liu, M., Stein, S., Wang, H., 2011. 2000 years of migrating earthquakes in North China: How earthquakes in midcontinents differ from those at plate boundaries, Geol. Soc. Am. 3, 128–132. https://doi.org/10.1130/L129.1

McCalpin, J.P., 2009. Paleoseismology, 2nd edition: International Geophysics Series, Academic Press, 613p.

Murray, A.S., Wintle, A.G., 2000. Luminescence dating of quartz using an improved single-aliquot regenerative-dose protocol. Rad. Meas. 32, 57–73.

Murray, A.S., Wintle, A.G., 2003. The single aliquot regenerative dose protocol: potential for improvements in reliability. Rad. Meas. 37, 377–381. https://doi.org/10.1016/S1350-4487(99)00253-X

Nanjo, K.Z., Izutsu, J., Orihara, Y., Kamogawa, M., Nagao, T., 2019. Changes in Seismicity Pattern Due to the 2016 Kumamoto Earthquakes Identify a Highly Stressed Area on the Hinagu Fault Zone. Geophys. Res. Lett. 46, 9489–9496. https://doi.org/10.1029/2019GL083463

Okada, A., Watanabe, M., Sato, H., Jun, M.S., Jo, W.R., Kim, S.K., Jeon, J.S., Chi, H.C., Oike, K., 1994. Active fault topography and trench survey in the central part of the Yangsan fault, south Korea. J. Geograp. 103, 111–126 (in Japanese).

Okada, A., Watanabe, M., Suzuki, Y., Kyung, J.-B., Jo, W.-R., Kim, S.-K., Oike, K., Nakamura, T.,1998. Active Fault Topography and Fault Outcrops in the Central Part of the Ulsan Fault System, Southeast Korea. J. Geograp. 107, 644-658. https://doi.org/10.5026/jgeography.107.5_644

Okada, A., Takemura, K., Watanabe, M., Suzuki, Y., Kyung, J.-B., Chae, Y.-H., Taniguchi, K., Ishiyama, T., Kawabata, D., Kaneda, H., Naruse, T., 1999. Trench excavation survey across the Ulsan (active) Fault at Kalgok-ri, Kyongju city, southeast of Korea. J. Geograp. 108, 276–288 (in Japanese with English abstract).

O'Neill, C., Müller, D., Steinberger, B., 2005. On the uncertainties in hot spot reconstructions and the significance of moving hot spot reference frames. Geochem., Geophys., Geos. 6, Q04003. https://doi.org/10.1029/2004GC000784

Park, J.C., Kim, W., Chung, T.W., Baag, C.E., Ree, J.H., 2007. Focal mechanism of recent earthquakes in the Southern Korean Peninsula. Geophys. J. Int. 169, 1103–1114.

https://doi.org/10.1111/j.1365-246X.2007.03321.x

Park, Y., Ree, J.-H., Yoo, S.-H., 2006. Fault slip analysis of Quaternary faults in southeastern Korea. Gondwana Res. 9, 118–125. https://doi.org/10.1016/j.gr.2005.06.007

Ramsey, C.B., 2009. Bayesian analysis of radiocarbon dates. Rad. 51, 337–360. https://doi.org/10.1017/S0033822200033865

Ramsey, C.B., 2017. Methods for summarizing radiocarbon datasets. Rad. 1–25. https://doi.org/10.1017/RDC.2017.108

Reimer, P. J., Austin, W. E. N., Bard, E., Bayliss, A., Blackwell, P. G., Bronk Ramsey, C., Butzin, M., Cheng, H., Edwards, R. L., Friedrich, M., Grootes, P. M., Guilderson, T. P., Hajdas, I., Heaton, T. J., Hogg, A. G., Hughen, K. A., Kromer, B., Manning, S. W., Muscheler, R., . . . Talamo, S., 2020. The IntCal20 Northern Hemisphere Radiocarbon Age Calibration Curve (0–55 cal kBP). Rad. 62, 725–757. https://doi.org/10.1017/RDC.2020.41

Rockwell, T., Ragona, D., Seitz, G., Langridge, R., Aksoy, M.E., Ucarkus, G., Ferry, M., Meltzner, A.J., Klinger, Y., Meghraoui, M., Satir, D., Barka, A., Akbalik, B., 2009. Palaeoseismology of the North Anatolian Fault near the Marmara Sea: implications for fault segmentation and seismic hazard. Geol. Soc. Spec. Publ. 316, 31–54. https://doi.org/10.1144/SP316.3

Scharer, K., Weldon II, R., Streig, A., Fumal, T., 2014, Paleoearthquakes at Frazier Mountain, California delimit extent and frequency of past San Andreas Fault ruptures along 1857 trace. Geophys. Res. Let. 41, 4527-4534. https://doi.org/10.1002/2014GL060318

Schellart, W.P., Rawlinson, N., 2010. Convergent plate margin dynamics: New perspectives from structural geology, geophysics and geodynamic modelling. Tectonophysics 483, 4–19. https://doi.org/10.1016/j.tecto.2009.08.030

Schwartz, D.P., Coppersmith, K.J., 1984. Fault Behavior and Characteristic Earthquakes: Examples from the Wasatch and San Andreas Fault Zone. J. Geophys. Res. 89, B7, 5681–5698. https://doi.org/10.1029/JB089iB07p05681

Schwartz, D.P., Haeussler, P.J., Seitz, G.G., Dawson, T.E., 2012. Why the 2002 Denali fault rupture propagated onto the Totschunda fault: Implications for fault branching and seismic hazards. J. Geophys. Res. Solid Earth 117(B11). https://doi.org/https://doi.org/10.1029/2011JB008918

Song, Y., Ha, S., Lee, S., Kang, H.-C., Choi, J.-H., Son, M., 2020. Quaternary structural characteristics and paleoseismic interpretation of the Yangsan Fault at Dangu-ri, Gyeongju-si, SE Korea, through trench survey. J. Geol. Soc. Kor. 56, 155–173 (in Korean with English abstract).

Thatcher, W., Rundle, J.B., 1979. A model for the earthquake cycle in underthrust zones. J. Geophys. Res. 84(B10), 5540–5556. https://doi.org/10.1029/JB084iB10p05540

Vallage, A., Klinger, Y., Lacassin, R., Delorme, A., Pierrot-Deseilligny, M., 2016. Geological structures control on earthquake rupture: The Mw 7.7 (2013). Balochistan earthquake, Pakistan. Geophys. Res. Lett. 43, 10155–10163. https://doi.org/10.1002/2016GL070418

Vallée, M., Landès, M., Shapiro, N. M., Klinger, Y., 2008. The 14 November 2001 Kokoxili (Tibet) earthquake: High-frequency seismic radiation originating from the transitions between sub-Rayleigh and supershear rupture velocity regimes. J. Geophys. Res. Solid Earth 113(B7). https://doi.org/https://doi.org/10.1029/2007JB005520

Wesnousky, S.G., 2008. Displacement and geometrical characteristics of earthquake surface ruptures: Issues and implications for seismic-hazard analysis and the process of earthquake

rupture. Bull. Seis. Soc. Am. 98(4) 1609–1632. https://doi.org/10.1785/0120070111

Williams, R.T., Goodwin, L.B., Sharp, W.D., Mozley, P.S., 2017. Reading a 400,000-year record of earthquake frequency for an intraplate fault. Proceedings of the National Academy of Sciences 114, 4893-4898. https://doi.org/doi:10.1073/pnas.1617945114

Wright, V., Woodcock, N.H., Dickson, J.A.D., 2009. Fissure fills along faults: Variscan examples from Gower, South Wales. Geol. Mag. 146(60), 890–902. https://doi.org/10.1017/S001675680999001X

Yin, A., 2010. Cenozoic tectonic evolution of Asia: A preliminary synthesis. Tectonophysics, 488, 293–325. https://doi.org/10.1016/j.tecto.2009.06.002

Zielke, O., Klinger, Y., Arrowsmith, J.R., 2015. Fault slip and earthquake recurrence along strike-slip faults — contributions of high-resolution geomorphic data. Tectonophysics 638, 43–62. https://doi.org/10.1016/j.tecto.2014.11.004

Figure captions

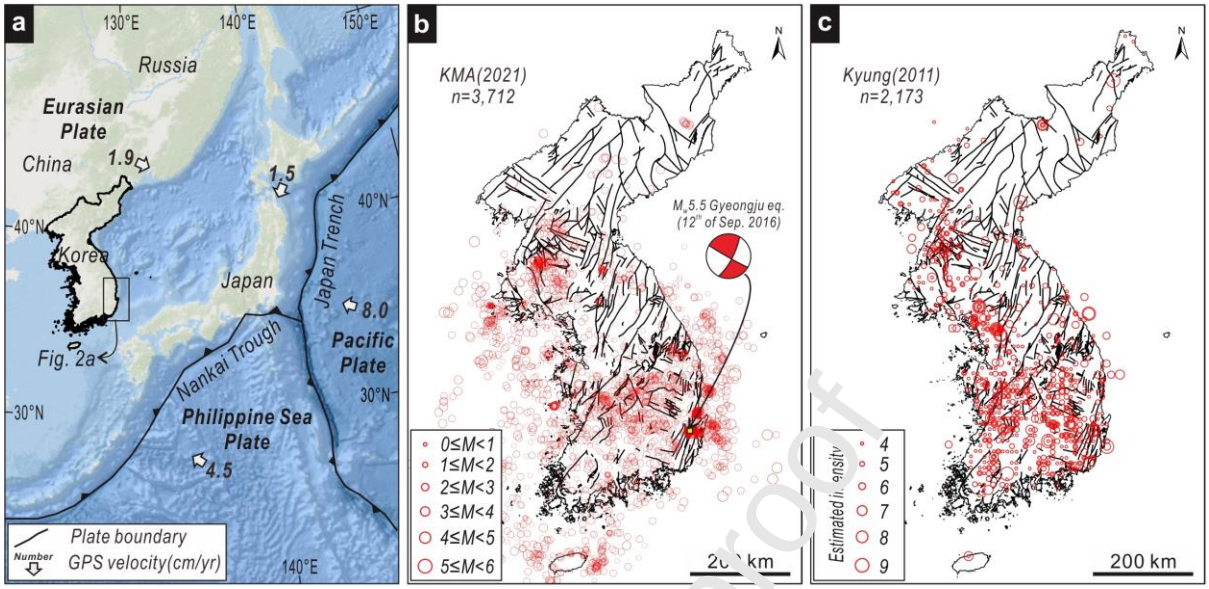

Fig. 1. (a) Present-day tectonic map of eastern Asia and their plate velocities (modified from Schellart and Raawlinson, 2010). The presented plate velocities are relative plate velocities (DeMets et al., 1994) according to the Indo-Atlantic hotspot reference frame (O'Neill et al., 2005). (b) Epicenter distributions of instrumental seismic records (modified from KMA, 2021; events from 1978 to 2021). The focal mechanism represents the Gyeongju earthquake (12 September 2016). (c) Estimated locations and intensities of historical earthquakes between CE 2 and 1904 (modified from Kyung, 2011).

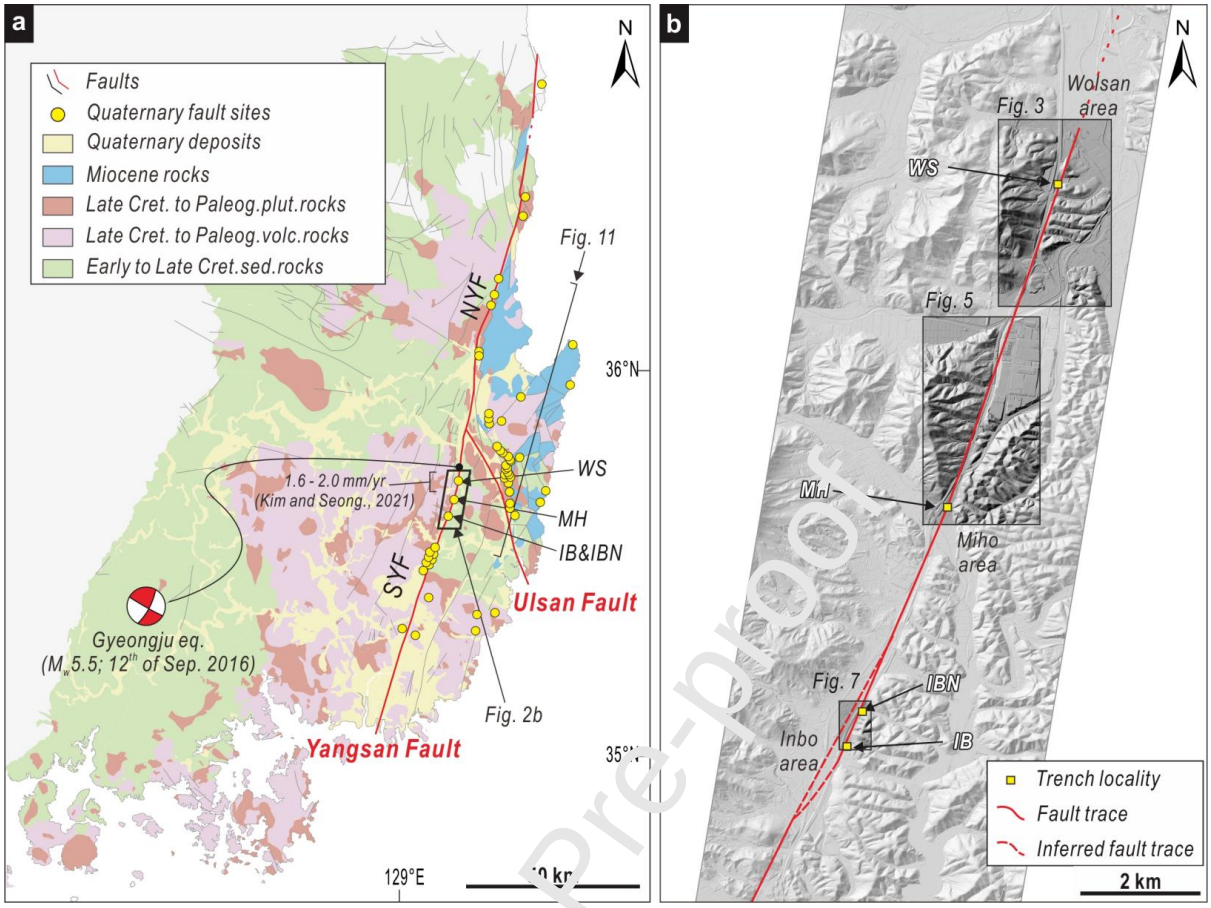

Fig. 2. (a) Simplified geological map of the southeastern Korean Peninsula, showing the distribution of major faults (modified after Chough and Sohn, 2010; NYF: northern Yangsan Fault; SYF: southern Yangsan Fault). The focal mechanism represents a recent moderate earthquake (Gyeongju Earthquake, 12 September 2016) along the Yangsan Fault. (b) Hill-shaded imagery (0.5 meter per pixel resolution) of the northern part of the SYF derived from LiDAR DEM (from 2017), showing the trace of the Yangsan Fault and trench survey locations (WS: Wolsan, MH: Miho, IBN: Inbo north, and IB: Inbo; from Cheon et al., 2020a) as well as areas of detailed geomorphic analysis (rectangles).

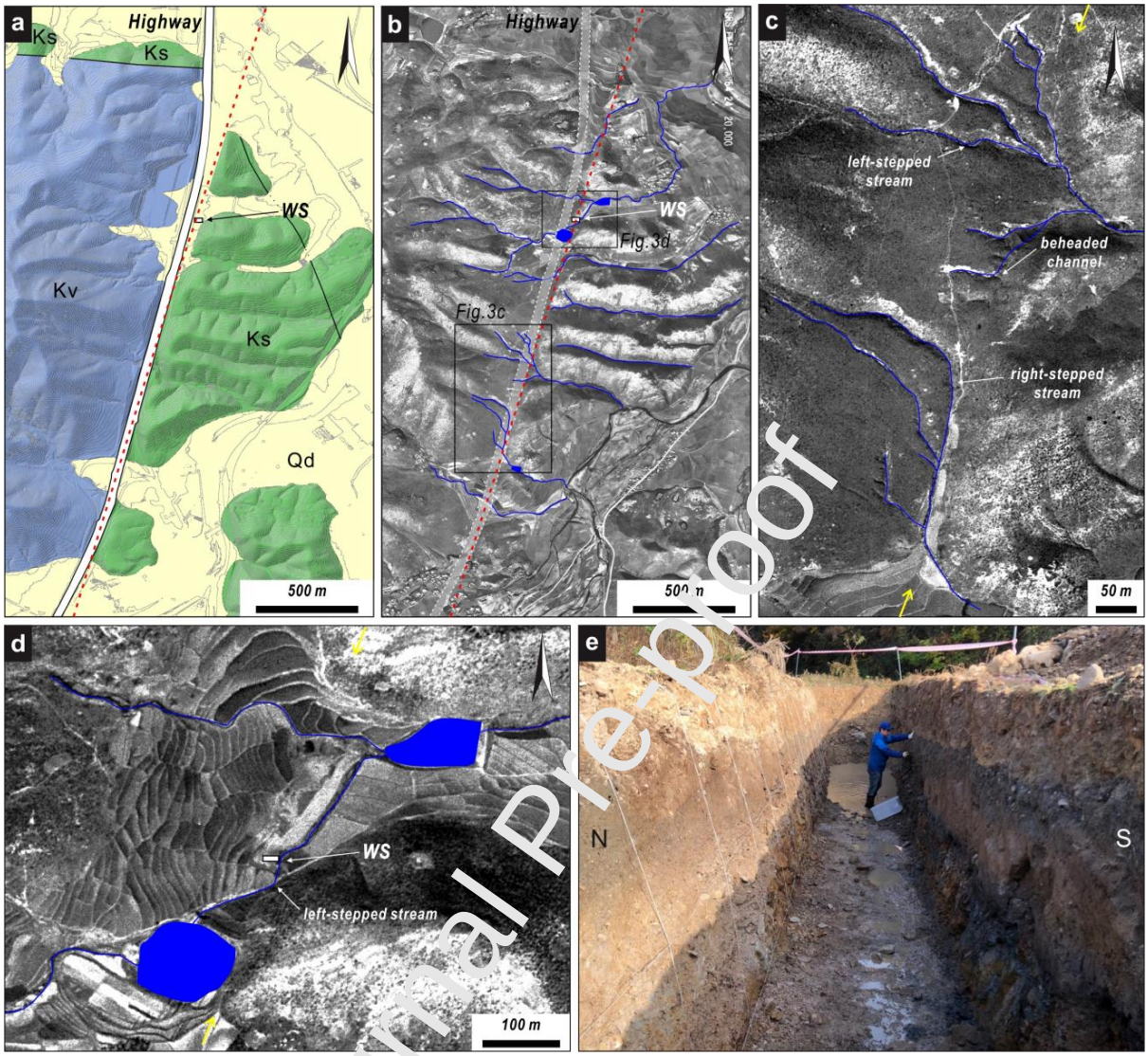

Fig. 3. Geology, faults, and geomorphology of the Wolsan area. (a) Geological map (modified from Lee et al., 2020; Kv: Cretaceous volcanic tuff, Ks: Cretaceous sedimentary rock, Qd: Quaternary deposit, solid/dashed black lines: neighboring faults, red dashed line: recently reactivated YF line) overlain on hill-shaded imagery from LiDAR data (from 2017). (b) Aerial photograph (from 1954) showing geomorphic features (the white rectangle marks the trench location). (c–d) Detailed geomorphic evidence for the inferred fault trace on the YF. Gullies are dextrally or sinistrally deflected along the fault line, which is represented by the NNE–SSW-striking, narrow, incised valley. (e) Photograph of the WS trench.

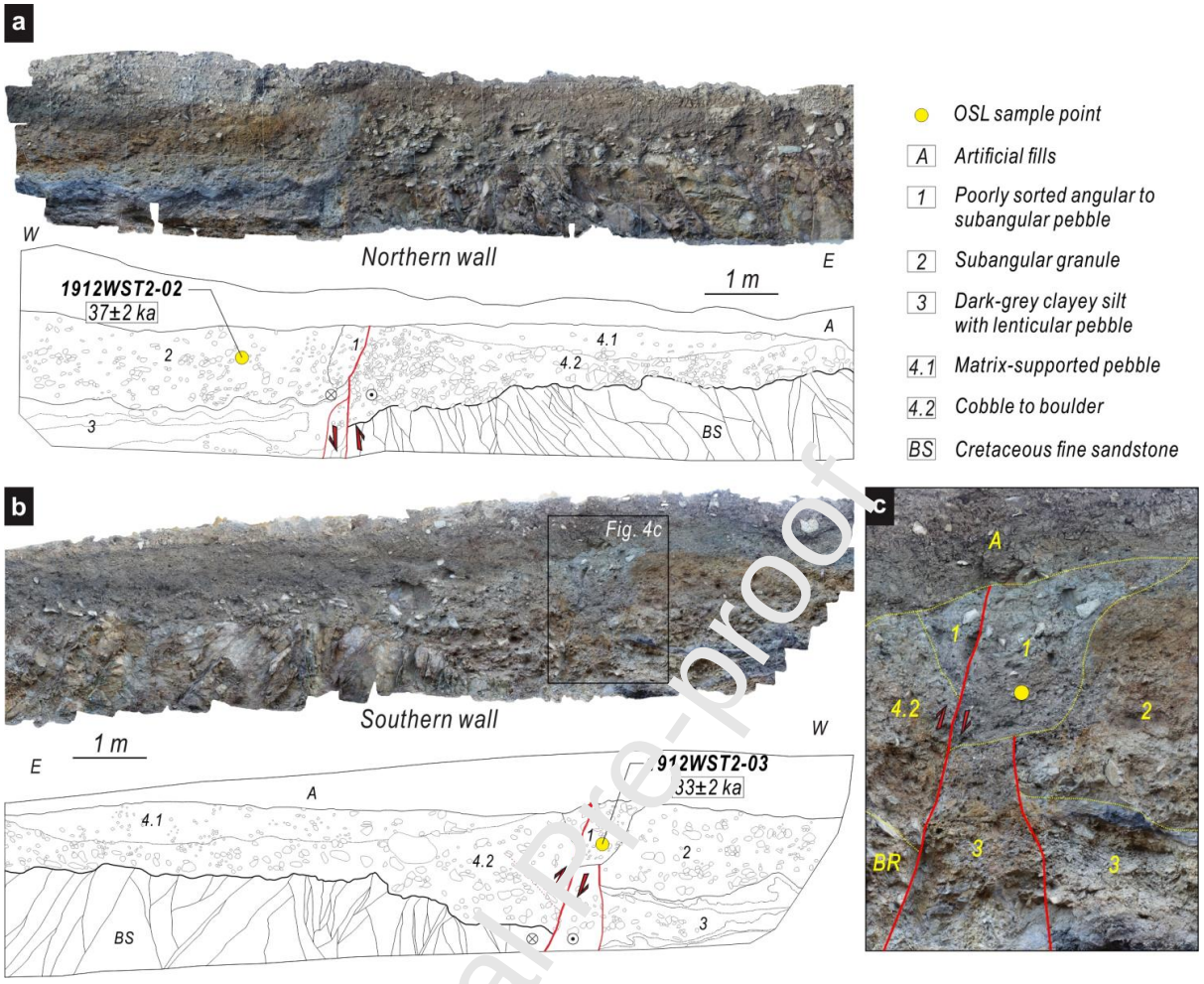

Fig. 4. Photographs and detailed trench logs of the northern (a) and southern (b) walls of the WS trench. The grid interval is 1 m × 1 m. Yellow circles indicate OSL sampling locations with ages. (c) The displaced fissure-fill deposit (unit 1) suggests that two events may be recorded in the trench.

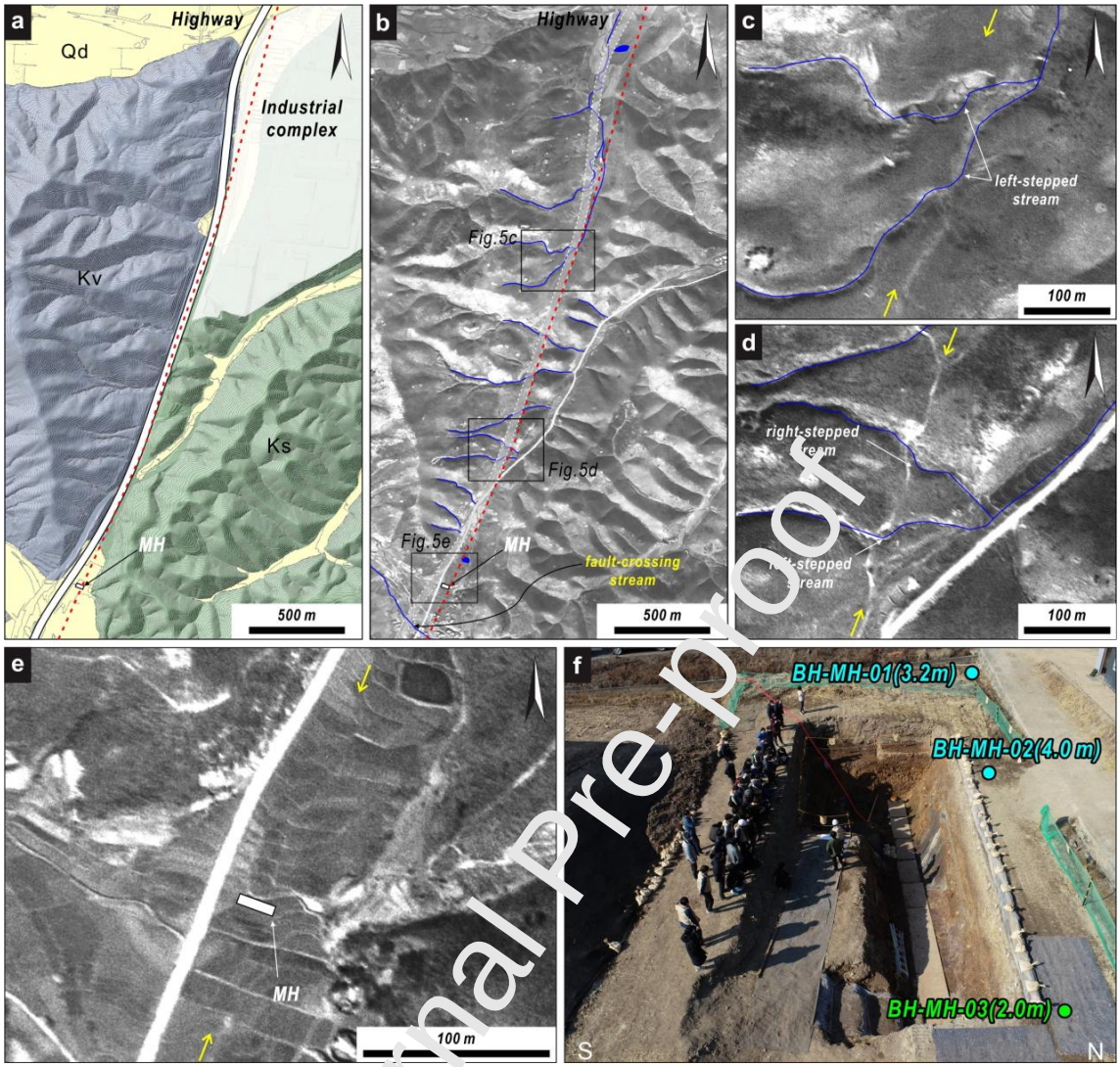

Fig. 5. Geology, faults, and geomorphology of the Miho area. (a) Geological map (modified from Lee et al., 2020; Kv: Cretaceous volcanic tuff, Ks: Cretaceous sedimentary rock; Qd: Quaternary deposit; red dashed line: recently reactivated YF line) overlain on hill-shaded imagery from LiDAR data (from 2017). (b) Aerial photograph (from 1954) showing geomorphic features (the white rectangle marks the trench location). (c–e) Dextrally or sinistrally deflected streams along the YF. (f) Photograph of the MH trench showing three borehole locations (BH-MH-01–03). Cyan and green circles represent Cretaceous dacitic welded tuff and fault rock derived from Cretaceous sedimentary rock, respectively. Numbers in parentheses near boreholes indicate depths to the unconformity between basement rock and overlying sediments.

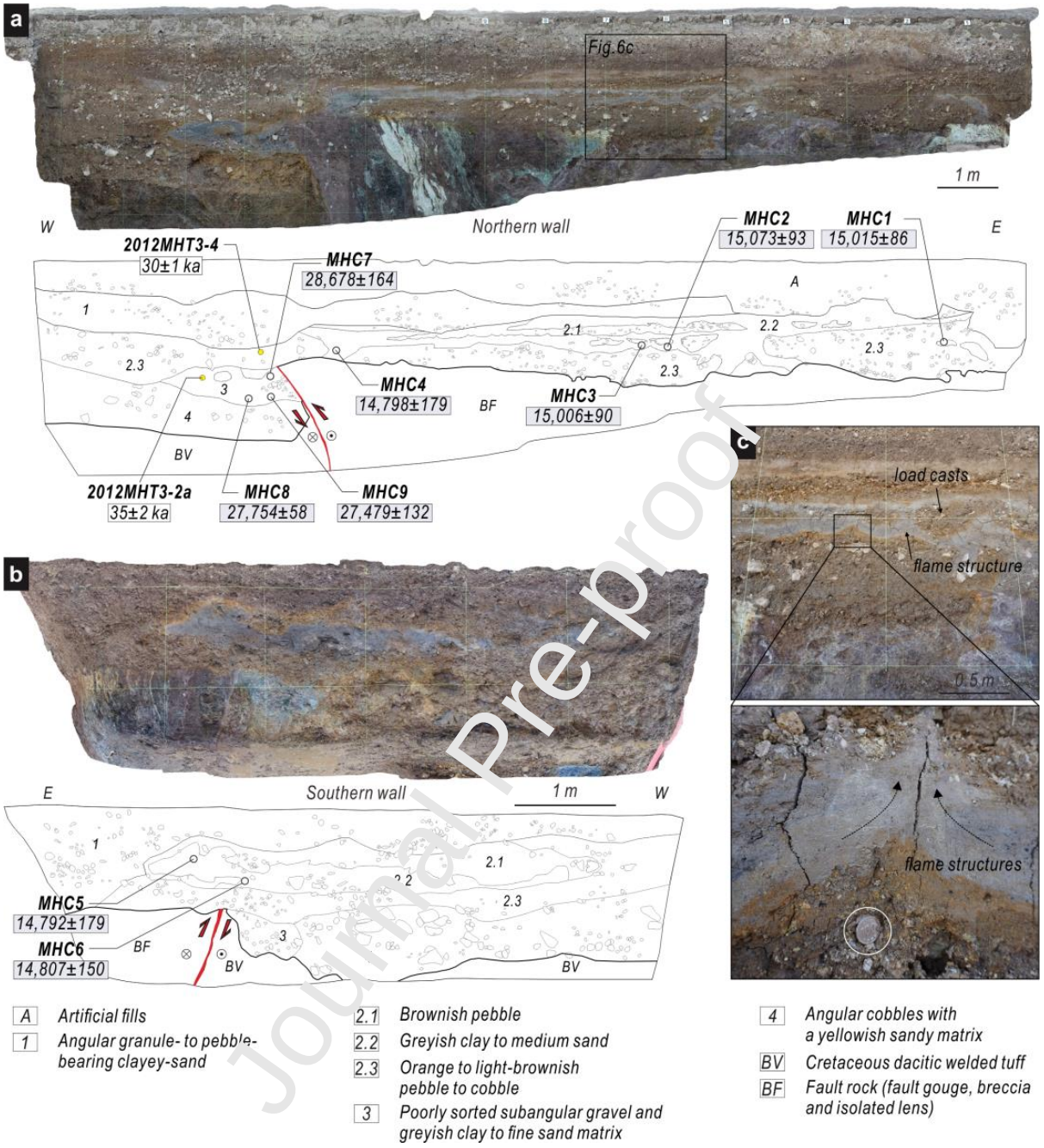

Fig. 6. Photographs and detailed sketches of the northern (a) and southern (b) walls of the MH trench. The grid interval is 1 m × 1 m. Yellow circles indicate OSL sampling points with ages with white background. White circles represent ^{14}C sample points with ages with grey background.

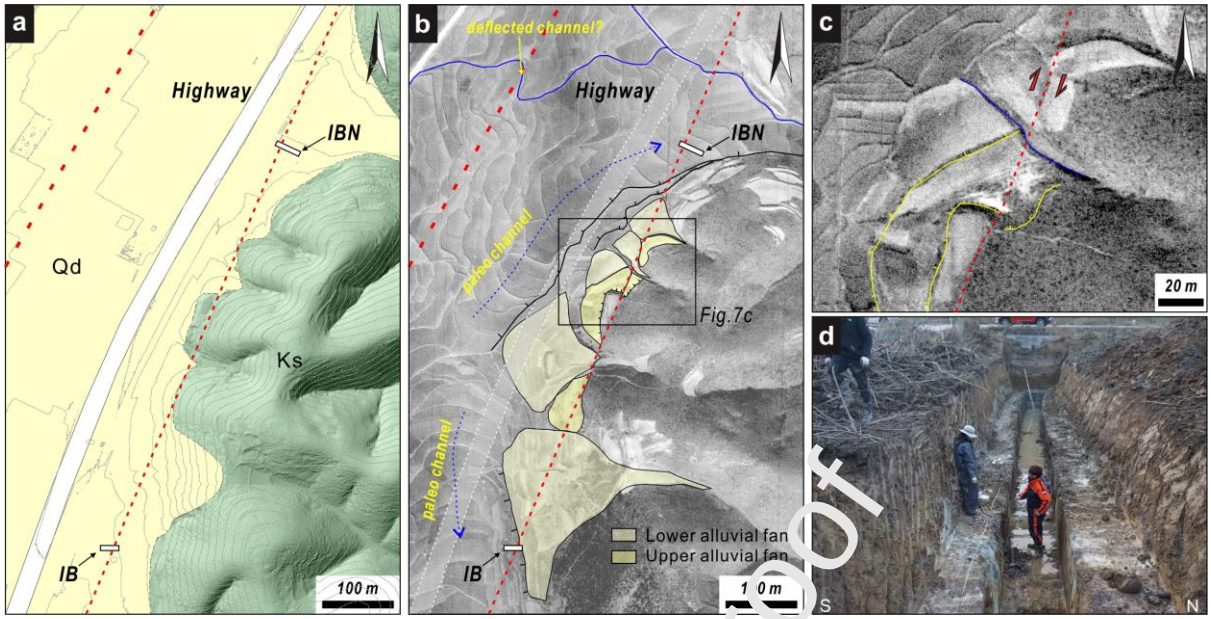

Fig. 7. Geology, faults, and geomorphology of the Ibo area. (a) Geological map (modified from Lee et al., 2020; Ks: Cretaceous sedimentary rock, Qd: Quaternary deposit); red dashed line: recently reactivated YF line) overlain on hill-shaded imagery from LiDAR data (from 2017). (b) Aerial photograph (from 1954) showing geomorphic features (the white rectangle marks the trench location). (c) Gullies and alluvial fans dextrally deflected along the inferred fault strand. (d) Photograph of the IBN trench.

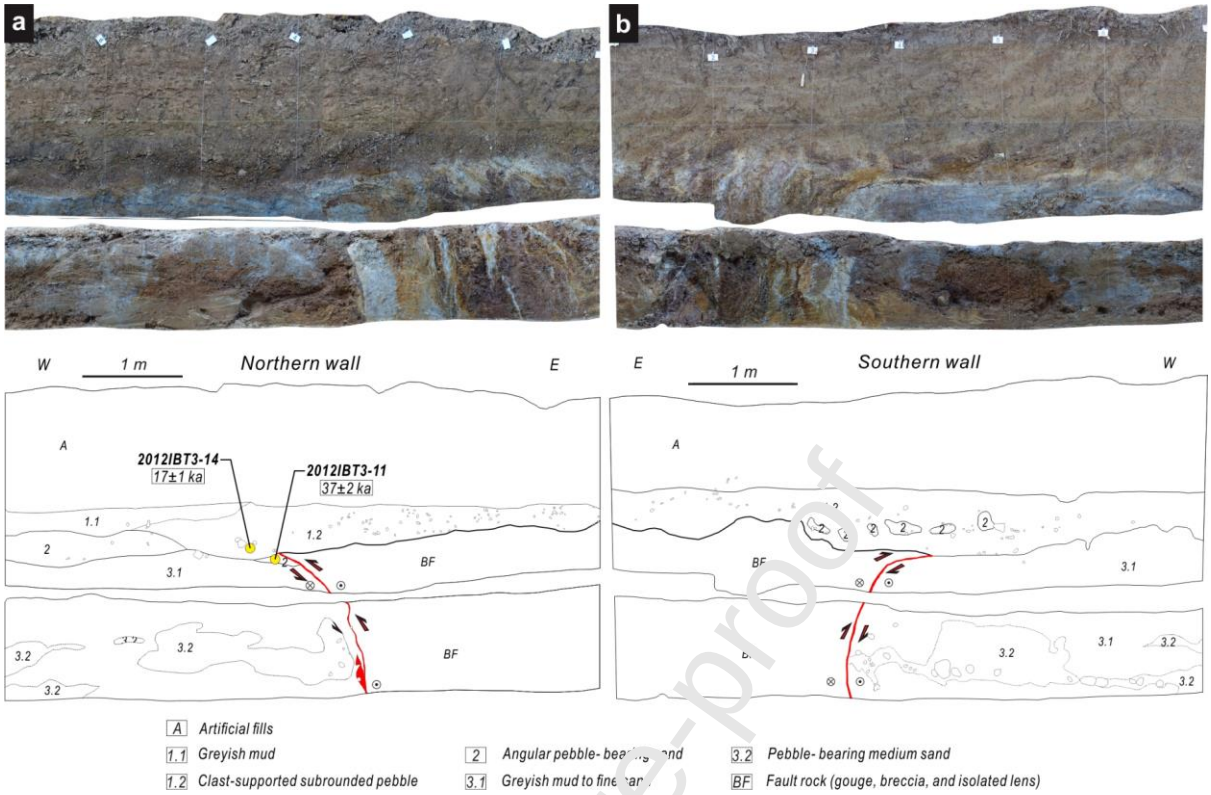

Fig. 8. Photographs and detailed sketches of the northern (a) and southern (b) walls of the IBN trench. The grid interval is 1 m × 1 m. Yellow circles indicate OSL sampling points with ages.

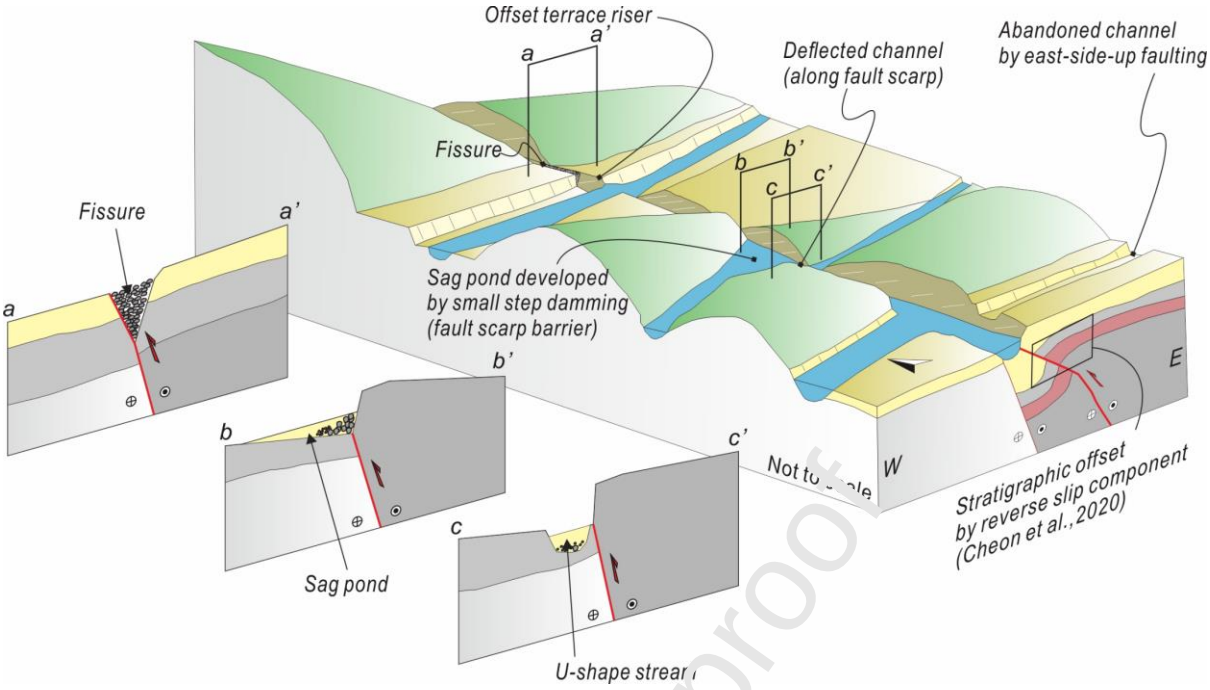

Fig. 9. Schematic diagrams showing landforms and stratigraphic features associated with strike-slip ruptures. A fissure-filling deposit is observed in the WS trench (profile a–a′). A sag pond deposit developed by fault scarp damming is observed in the northern wall of the MH trench (b–b′). A U-shaped cut-and-fill deposit along the fault splay is observed in the southern wall of the MH trench (c–c′ profile).

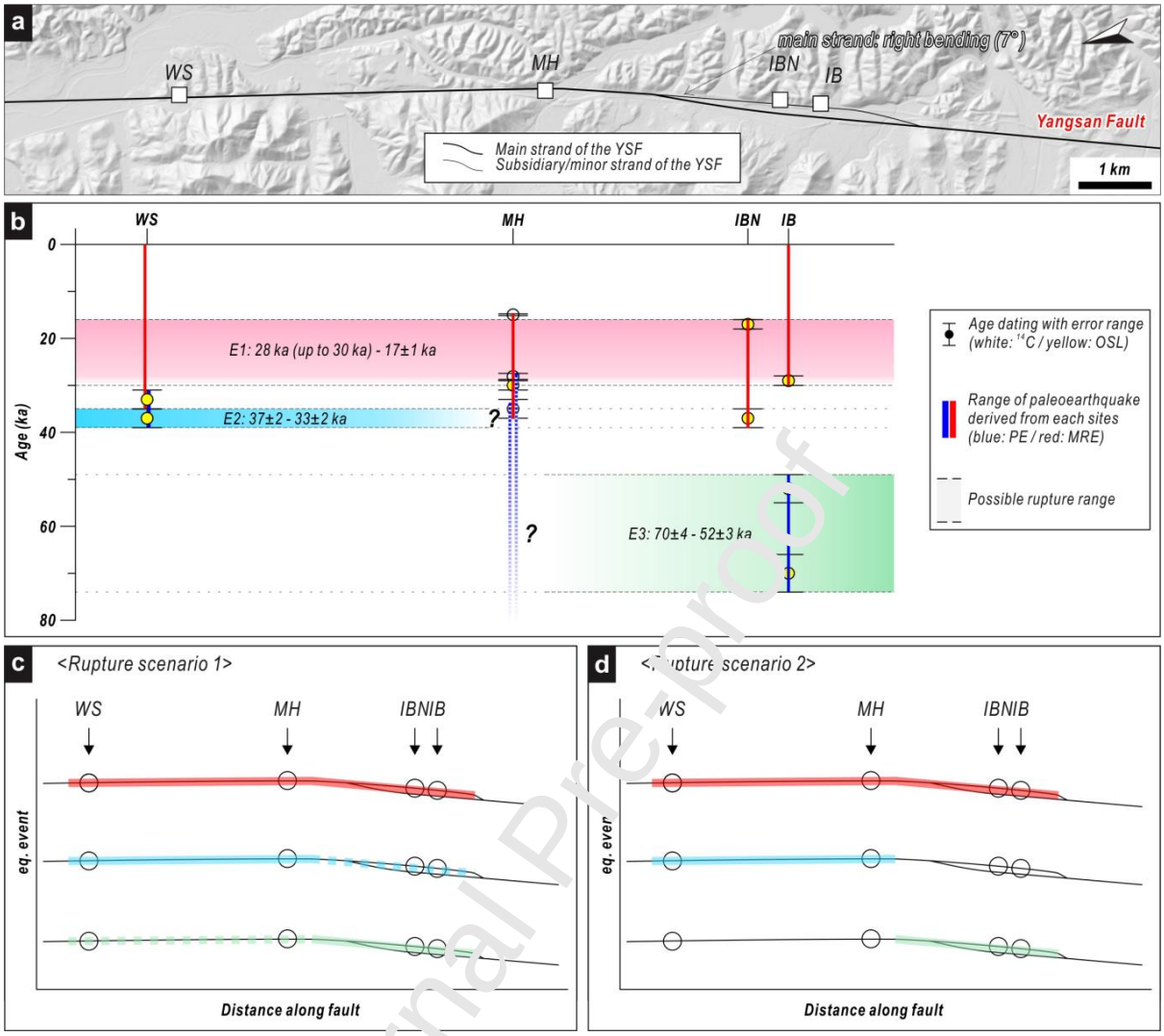

Fig. 10. Two possible rupture scenarios based on the timings of the MRE and PE along the studied sections of the SYF. (a) Spatial distribution of the studied sites and interpreted paleo-rupture map. (b) The timings of rupture from each trench site suggest that two or three surface-rupturing paleoearthquakes have occurred along the studied part of the SYF. (c–d) Two possible rupture scenarios for the studied part of the SYF: (c) Three surface-rupturing earthquakes occurred over the whole length of the studied part of the SYF, as in the "characteristic earthquake model" of Schartz and Coppersmith (1984). (d) The entire studied part of the SYF slipped during the MRE after two moderate-sized earthquakes had previously occurred at the WS–MH and IBN–IB sections, respectively, as in the "uniform slip model" of Schartz and Coppersmith (1984).

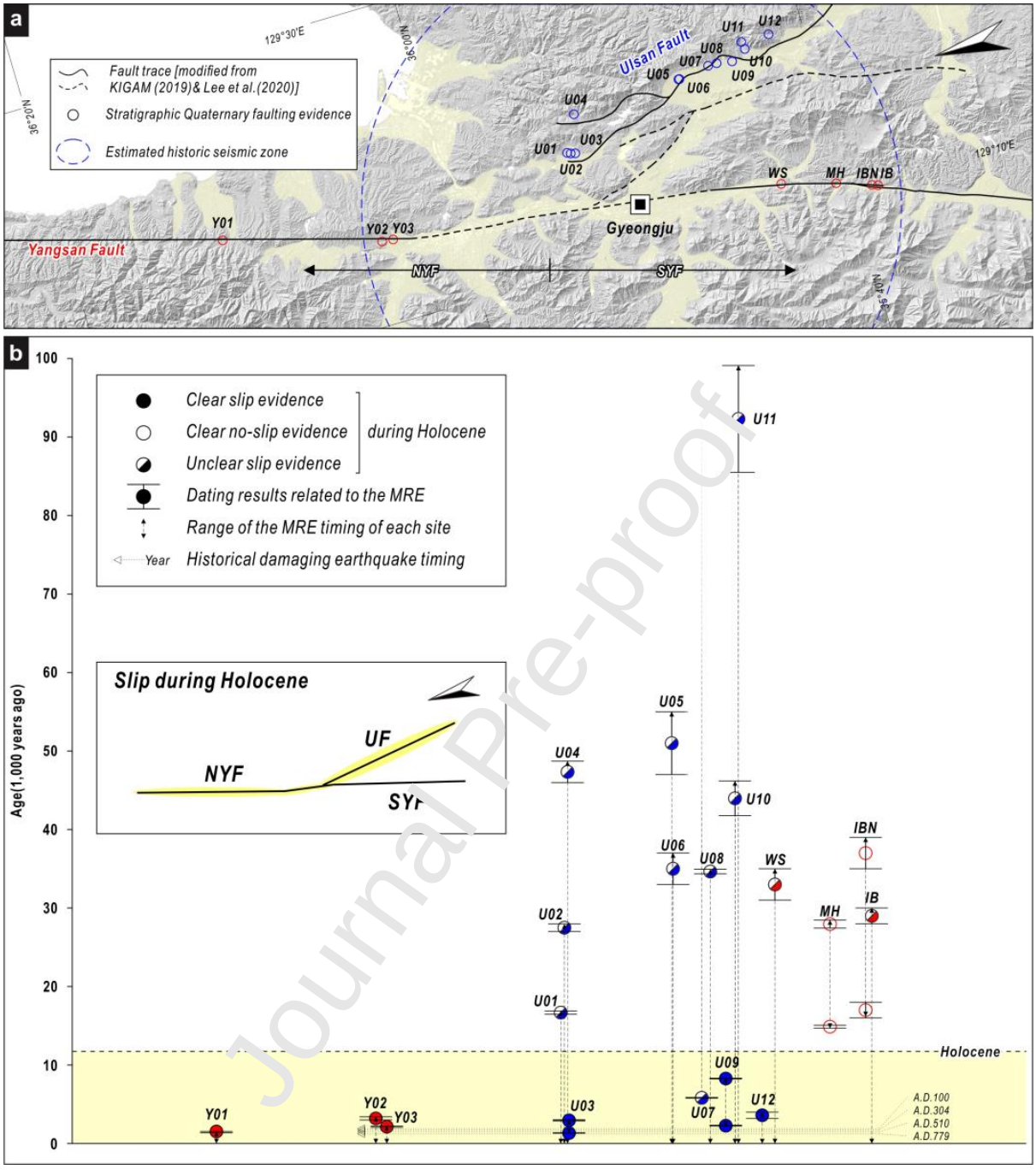

Fig. 11. Fault trace map (modified from Kee et al., 2019; Lee et al., 2020) and the timings of the MRE at sites along the YF and UF [Table S1; (U08) Okada et al., 1998; (U02) Okada et al., 1999; (U01 and U09) Inoue and Choi, 2006; (Y01 and U03) Kyung, 2010; (U04, U10, and U11) Choi et al., 2012b; (U05 and U06) Choi et al., 2014; (Y03) Cho et al., 2016; (IB) Cheon et al., 2020a; (U07) Kim et al., 2020; (Y02) Song et al., 2020; (U12) Kim et al., 2021; (WS, MH, and IBN) this study]. Locations of historically recorded damaging earthquakes (CE 100,

304, 510, and 779) near Gyeongju City are contained in the dashed blue circle. (b) Stratigraphic evidence for surface rupturing during the Holocene reported along the NYF and UF (yellow-shaded area in the inset diagram). Depending on the relationship between historical earthquake events and faulting location, the surface rupturing can be interpreted in terms of two possible faulting scenarios. See Section 5.2 for a detailed explanation.

Tables

Table 1. *Water contents, dose Rates, D_e values, and OSL ages of analyzed samples.*

Sample[a]	Water (wt.%)	Beta dose[b] (Gy/Ka)	Gamma dose[b] (Gy/Ka)	Cosmic dose[b] (Gy/Ka)	Total dose rate[b] (Gy/Ka)	Qtz OSL D_e (Gy)	Qtz OSL Age[c] (Ka)	Aliquots used (*n*)
1912WST2-02	13.4	2.48 ± 0.15	1.39 ± 0.08	0.17 ± 0.01	4.04 ± 0.17	150.0 ± 5.6	**37 ± 2**	18
1912WST2-03	18.8	2.27 ± 0.13	1.30 ± 0.08	0.17 ± 0.01	3.74 ± 0.15	123.1 ± 5.7	**33 ± 2**	16
2012MHT3-02a	25.0	1.86 ± 0.10	1.11 ± 0.06	0.16 ± 0.01	3.12 ± 0.12	107.8 ± 3.2	**35 ± 2**	12
2012MHT3-04	16.9	2.18 ± 0.13	1.22 ± 0.07	0.17 ± 0.01	3.56 ± 0.13	108.2 ± 2.1	**30 ± 1**	12
2012IBT3-11	20.6	1.85 ± 0.11	1.05 ± 0.06	0.16 ± 0.01	3.06 ± 0.12	111.8 ± 3.2	**37 ± 2**	12
2012IBT3-14	15.0	1.67 ± 0.10	0.98 ± 0.06	0.17 ± 0.01	2.82 ± 0.12	47.0 ± 1.3	**17 ± 1**	12
IBTB-F-03 (personal communication with Lee, T.-H.)	17.3	1.58 ± 0.09	1.00 ± 0.06	0.17 ± 0.01	2.75 ± 0.11	143.9 ± 4.6	**52 ± 3**	16
IBT-01 (Cheon et al., 2020)	48	1.6 ± 0.1	1.2 ± 0.1	0.2 ± 0.0	2.9 ± 0.1	202.1 ± 8.1	**70 ± 4**	14
IBT-02 (Cheon et al., 2020)	24	2.1 ± 0.1	1.2 ± 0.1	0.1 ± 0.0	3.4 ± 0.2	237.7 ±7.6	**70 ± 4**	17
IBT-03 (Cheon et al., 2020)	18	1.6 ± 0.1	1.0 ± 0.1	0.2 ± 0.0	2.8 ± 0.1	80.5 ± 2.1	**29 ± 1**	12

[a]Coarse-grained (90–250 μm) quartz was used for OSL dating of each sample.

[b]Beta, gamma, cosmic dose, and total dose rates are rounded to two decimal places.

[c]Central age ± 1σ (1 standard error).

Table 2. *Results of calibrated radiocarbon age dating of samples from the Miho trench wall and weighted mean age using OxCal 4.4 (sample locations are shown in Fig. 5).*

Sample ID	Conventional radiocarbon age	Error	Calibrated age with 1σ error	Unit

	(^{14}C yr BP)		(^{14}C cal yr BP)	
MHC1	12,609	56	15,101–14,929	2.2N
MHC2	12,703	66	15,165–14,980	2.2N
MHC3	12,598	54	15,095–14,916	2.2N
MHC4	12,475	52	14,976–14,619	2.2N
MHC5	12,462	52	14,970–14,613	2.2S
MHC6	12,413	52	14,957–14,657	2.2S
Weighted mean of unit 2.2 radiocarbon dating: 14,887 ± 192 cal yr BP				
MHC7	24,448	122	28,841–28,514	3N
MHC8	23,580	80	27,811–27,696	3N
MHC9	23,210	80	27,611–27,247	3N
Weighted mean of unit 3 radiocarbon dating: 27,959 ± 51[illegible] cal yr BP				

Declaration of interests

☒ The authors declare that they have no known competing financial interests or personal relationships that could have appeared to influence the work reported in this paper.

☐ The authors declare the following financial interests/personal relationships which may be considered as potential competing interests:

Abstract

The construction of spatiotemporal models of earthquake occurrence for intraplate areas is challenging due to the low deformation rates in these areas. In this study, we conducted paleoseismological investigations along the southern Yangsan Fault (SYF), a typical low-deformation-rate fault, on the Korean Peninsula. The SYF is distinct from the northern Yangsan Fault (NYF), and the boundary between them is located at the junction between the NNE-striking YF and another major structure, the NNW-striking Ulsan Fault (UF), which branches off from the YF. Paleoseismological trenches at four sites along the SYF indicate that this fault section has not ruptured during the Holocene, in contrast to the NYF and UF. In detail, surface ruptures along the studied section of the SYF occurred during three different time periods, as inferred from stratigraphy and radiocarbon dating: 74 to 49 ka at two sites, 39 to 35 ka at another site, and 28,000 cal yr BP (or 30 ka considering the OSL age) to 16 ka at all sites. These results suggest two alternative rupture scenarios for the timing of paleoearthquakes along the studied fault section during the Late Pleistocene: (1) full rupture along the entire studied section during each earthquake event, or (2) multiple partial ruptures along the two structurally distinguishable parts of the studied fault section, that is, the Wolsan–Miho and Inbo north–Inbo sections. We conclude that geometric discontinuities of the long-lived YF system in the Korean Peninsula intraplate region have played an important role in controlling recent spatiotemporal rupture behavior.

Credit Author Statement

Taehyung Kim: Investigation, Writing - Original Draft **Jin-Hyuck Choi**: Conceptualization, Investigation, Writing - Review & Editing **Youngbeom Cheon**: Conceptualization, Investigation, Writing - Review & Editing, Supervision **Tae-Ho Lee**: Formal analysis, Writing - Original Draft **Namgwon Kim**: Investigation **Hoil Lee**: Investigation **Chang-Min Kim**: Investigation **Yire Choi**: Formal analysis **Hankyung Bae**: Investigation **Young-Seog Kim**: Writing - Review & Editing **Chung-Ryul Ryoo**: Investigation **Yann Klinger**: Writing - Review & Editing

Highlights

- The Yangsan Fault is a typical low-deformation-rate fault on the Korean Peninsula
- Late Pleistocene rupture scenarios for the southern Yangsan Fault are proposed
- Geometric discontinuities play an important role in controlling rupture behavior